Adipose tissue-derived fibroblasts engage in immune-stromal crosstalk during obesity-aggravated atherosclerosis in mice

Authors
Mikkola Lea, PhD, Turku Bioscience Centre, InFLAMES Research Flagship Centre, University of Turku, Turku, Finland
Bölük Aydin, MD, A.I. Virtanen Institute for Molecular Sciences, University of Eastern Finland, Kuopio, Finland
Piipponen Minna, PhD, Turku Bioscience Centre, InFLAMES Research Flagship Centre, University of Turku, Turku, Finland
Mikocziova Ivana, PhD, Turku Bioscience Centre, InFLAMES Research Flagship Centre, University of Turku, Turku, Finland
Valkonen Mira, PhD, Institute of Biomedicine, University of Turku, Turku, Finland, and Faculty of Medicine and Health Technology, University of Tampere, Tampere, Finland
Fagersund Jimmy, MSc, Turku Bioscience Centre, University of Turku, Turku, Finland
Hakovirta Harri, MD, PhD, Heart Centre, Department of Vascular surgery, and University of Turku Department of Surgery, University Hospital of Turku, Turku, Finland
Saraste Antti, MD, PhD, Heart Centre, Turku University Hospital and University of Turku, Turku, Finland, and PET Centre, Turku University Hospital and University of Turku, Turku, Finland
Hernández de Sande Ana, PhD, Institute of Biomedicine, University of Eastern Finland, Kuopio, Finland
Palani Senthil, PhD, PET Centre, InFLAMES Research Flagship Centre, University of Turku, Turku, Finland
Örd Tiit, PhD, A.I. Virtanen Institute for Molecular Sciences, University of Eastern Finland, Kuopio, Finland
Roivainen Anne, PhD, PET Centre, InFLAMES Research Flagship Centre, University of Turku, Turku, Finland
Ruusuvuori Pekka, Institute of Biomedicine, University of Turku, Turku, Finland, and Faculty of Medicine and Health Technology, University of Tampere, Tampere, Finland
Heinäniemi Merja, PhD, Institute of Biomedicine, University of Eastern Finland, Kuopio, Finland
Kaikkonen U. Minna, PhD, A.I. Virtanen Institute for Molecular Sciences, University of Eastern Finland, Kuopio, Finland
Lönnberg Tapio, PhD, Turku Bioscience Centre, InFLAMES Research Flagship Centre, University of Turku, Turku, Finland

Corresponding authors:
Lönnberg Tapio, taplon@utu.fi, Tykistökatu 6 A, 20520, Turku, Finland
Mikkola Lea, limikk@utu.fi, Tykistökatu 6 A, 20520, Turku, Finland

Abstract

Background

Atherosclerosis is a common disorder where changes in vascular wall and in the surrounding perivascular adipose tissue are evident. However, how multiple cell types contribute to the disease at the cellular level remains poorly understood. Moreover, obesity can exacerbate atherogenesis, but it remains to be revealed which cell types drive the aggravation.

Our objectives were to define the key cell populations across tissues in a highly atherogenic mouse model of atherosclerosis under obese and normal-weight conditions, and to explore tissue-specific cellular changes and interactions associated with obesity.

Methods

We employed 5' single-cell RNA sequencing combined with antibody staining in $Ldlr^{-/-}$ $Apob^{100/100}$ male mice, comparing two groups: animals fed a high-fat diet to induce obesity and those maintained on regular chow as non-obese controls. We harvested aorta, epididymal and perivascular adipose tissues, and spleen from each animal. Aorta samples were CD45+ enriched, and a panel of 138 antibodies was used to generate CITE-seq libraries. Spatial transcriptomics of human carotid arteries and aorta were used to confirm the expression of top targets from the mouse model. Immunohistochemistry and multiplexed immunofluorescence were used to validate the findings.

Results

We generated data from almost 46000 cells enabling analyses of cell phenotypes, gene set enrichment, regulon activity, and cell interactions. We found fibroblast subpopulations derived from the adipose tissues to be involved in local immune responses and potential contributors to atherosclerosis in obesity. *Pi16*+ progenitor fibroblasts were significantly reduced and PVAT morphology was remarkably changed in obesity. We also observed clear spatial patterning of the top differentially expressed genes from our mouse model in human aorta and carotid artery.

Conclusions

We present a comprehensive multi-tissue single-cell analysis of the immune-stromal landscape in a murine model of atherosclerosis in obesity and normal state. Fibroblasts show distinct immune activation especially in perivascular adipose tissue.

Introduction

Atherosclerosis is one of the pervasive common complex disorders that is greatly impacted by genetic components. Large genome-wide association studies have identified hundreds of risk loci but their predictive power and especially understanding of the disease mechanisms is still limited[1]. Single-cell and spatial omics (e.g. transcriptomics, proteomics and epigenetics) studies have expanded in recent years to enable high-resolution profiling of cellular heterogeneity, in-depth investigation of transcriptional cell regulation, and cell-cell and cell-tissue microenvironment (TME) crosstalk in health and disease, including atherosclerosis[2]. Immune-structural cell interactions have been recognized to be pivotal for the maintenance of tissue homeostasis in healthy tissues and during disease states[3–5]. Especially fibroblasts have been under growing interest in atherosclerosis studies in the recent years [6]. Activated adventitial fibroblasts have been indicated as having multifaceted functions during atherosclerosis progression, for instance in proinflammatory signalling, extracellular matrix modulation, and immune cell recruitment via chemotaxis[6]. Switching off inflammatory programs is important after resolving an acute inflammation, and if this fails, chronic inflammation may occur. Fibroblasts that have lost their ability to switch away from the inflammatory program could be at the focal point of persistent inflammation[7].

Instead of concentrating on only immune cells and/or only on arterial tissues, our objectives were to map the immune-stromal landscape of multiple tissues and investigate the intricate cell interactions in an atherosclerosis mouse model to better understand the drivers of the disease during obesity. To this end, we generated data that included a wide variety of immune and non-immune cell types and multiple tissue types that might harbor cells crucial to the development of atherosclerosis. In addition to the whole aorta, we collected perivascular adipose tissue (PVAT), epididymal white adipose tissue (eWAT), and the whole spleen. Spleen was included due to its important role in lipid metabolism, homing and transforming of lymphocytes, macrophage activation, and potentially substantial participation in the atherosclerosis-associated immune responses [8–10]. Meanwhile, PVAT and eWAT were important target tissues because obesity has a major impact on the development of atherosclerosis, and it has been shown that both the white adipose tissue, especially in the visceral depots, and PVAT may convert to a proinflammatory phenotype during obesity induced by caloric intake excess[11–13]. Our data included samples from both obese and non-obese mice (Fig. 1A) that had been fed either a high-calorie or normal chow diet for three months, thus modelling the effect of caloric intake excess on the development of atherosclerosis.

We have constructed a uniquely diverse multi-tissue single-cell data of atherosclerosis murine models representing the disease states during obesity and normal body weight, which enabled the mapping of the most pivotal cell types and changes in their gene expression profiles, as well as study of their regulons and cell interactions. We found that perivascular and white adipose tissue fibroblasts have been drastically impacted by obesity in this atherosclerosis model. Moreover, we showed that in addition to strong potential in interactions with immune cells, some of these fibroblasts demonstrated marked immune-regulation potential that has not been described previously in the context of atherosclerosis and obesity.

Methods

Data availability

The single-cell RNA sequencing data is available in the Gene Expression Omnibus database (GSE235895). Due to data sensitivity, the spatial transcriptomics data of human samples is not available via open repositories, but the non-sensitive count matrices can be shared to trusted parties on request from VarHa (wellbeing services county of Southwest Finland) research centre.

IHC-based cell counting data of PI16+ fibroblasts is available at 10.6084/m9.figshare.28956140, and the data for the morphometric analysis at 10.6084/m9.figshare.28956104. Original images of CD19 and CD74 antibody staining on mouse PVAT-aorta are available at 10.6084/m9.figshare.29279045 (CD19) and 10.6084/m9.figshare.30030004 (CD74). Human aorta and carotid artery H&E, CD68 and CD206 staining images are available at 10.6084/m9.figshare.30016450.

Animals

Animal experiments were approved by the National Experiment Animal Board of Finland (permission numbers ESAVI/4567/2018, ESAVI/6772/2018, and ESAVI/17197/2021) and were carried out in accordance with the Finnish Act on Animal Experimentation and EU Directive 2010/EU/63 on the protection of animals used for scientific purposes.

Sample collection and processing for single-cell transcriptomics

A total of ten male mice lacking Ldlr and solely expressing ApoB100 ($Ldlr^{-/-}$ / $ApoB^{100/100}$, C57BL/6J background; strain 003000, Jackson Laboratory) were bred and housed at the University of Turku Central Animal Laboratory (Turku, Finland). Mice fed with high fat diet (TD.88137, Envigo, US) for 3.5 months represented obese or atherosclerotic model (n=5) and mice fed with regular chow diet represented non-obese state or controls (n=5). The mice were age matched at the time of the sacrifice. The mice were first anesthetized by isoflurane (induction 4-5 %, maintenance 2-2.5 %), followed by drawing of the blood with cardiac puncture, after which the animals were euthanized with cervical dislocation. Each mouse was perfused with ice-cold 10 ml DPBS (L0615-500, Biowest, Nuaillé, France) including 10 U/ml heparin (C29859, LEO Pharma, Ballerup, Denmark) before further dissection.

Four different tissues were collected: aorta (incl. the aortic tissues from ascending aorta until the renal arteries branch from the abdominal aorta), perivascular adipose tissue surrounding the aorta, epididymal white adipose tissue, and spleen. The tissues were kept in DPBS on ice, they were individually weighed, and PVAT was separated from aortas on a cold block in a drop of DPBS. Single cell solutions were prepared from the four tissues by following the protocol specified in Figshare (10.6084/m9.figshare.29312777), including red blood cell lysis with ice-cold lysis buffer (eBioscience™ 10X RBC Lysis Buffer, 00-4300-54, Thermo Fisher Scientific, US). The same tissue types from all mice in the same group were pooled together from the beginning, except the aortas. The input quantities were equalized (for mass) to ensure similar proportions of each individual sample in the pooled sample. The aorta samples were pooled after dissociation. The cell concentration and viability of the resulting cell suspensions

were measured with a LUNA FX7 instrument (Logos Biosystems, South Korea) using acridine orange and propidium iodide stains. The viability varied between ~ 87-95 %, therefore no dead cell removal was needed for any of the samples.

A positive enrichment of CD45+ cells was carried out using a Miltenyi CD45 MicroBeads kit (mouse, 130-052-301) in the pooled aorta sample. The enrichment was done according to the Miltenyi protocol (140-003-515.01). Before enrichment 30 µl of the original sample was taken aside so it could be mixed with the enriched sample. This was done because the enriched sample is expected to be highly pure (> 90 % CD45+ cells) and we did not want to exclude all the CD45- cell types. A 20-25%:75-80% ratio was used for mixing the original and enriched sample, respectively. Next, the cells were stained with an experimental BioLegend Totalseq-C panel, containing 138 antibodies (10.6084/m9.figshare.29312825, file feature_bc_totseqC.csv), following the manufacturer's protocol (https://www.biolegend.com/en-us/protocols/totalseq-b-or-c-with-10x-feature-barcoding-technology) and continued to the single cell immune profiling protocol.

For validation experiments we got ten more mice from the Lab Animal Centre at the University of Eastern Finland. The mice were transferred to the mouse facilities of the University of Turku Central Animal Laboratory, and five of them were put on a high fat diet (TD.88137, Ssniff Spezialdiäten GmbH, Germany) for 3,5 months, while the other five were sacrificed at 6-month-old after being solely fed with chow (Teklad 2018c, Envigo, US). The same tissues were collected from the mice as in the original experiment. The samples were snap frozen in ethanol dry ice slurry and stored in -150°C for later use. Also, part of the samples were collected so that the PVAT was kept around the descending aorta. These AO-PVAT samples (approximately 10 mm in length) were collected rostrally just above the renal arteries, and were individually fixed with 4 % paraformaldehyde, dehydrated in 70 % EtOH, and paraffin embedded for immunohistochemistry (IHC) and multiplexed immunofluorescence (mIF) experiments.

TotalSeq antibody staining of cell surface proteins

From each tissue type, approximately 2.5x10^5 cells were used for surface staining, to be used as input material for the subsequent single-cell analysis. The cells were first incubated with anti-mouse CD16/CD32 (Clone 2.4G2) (InVivoMAb, PN-BE0307) 1:100 in 1% BSA-PBS for 10 minutes on ice to block Fc receptors. The lyophilized TotalSeq-C mouse custom cocktail panel (BioLegend, PN-900002539) was reconstituted following manufacturer's instructions. After blocking of the Fc receptors, the cell suspension was incubated with 12.5 µl of the TotalSeq-C panel and 75 µl of 1% BSA-PBS on ice for 30 minutes. After the antibody incubation, the cells were washed first once with 0.04% BSA-PBS and then twice with 1% BSA-PBS, pelleting the cells by centrifugation (400 x *g*, 5 min, +4°C) and removing supernatant between the washes. The cells were finally resuspended in 1% BSA-PBS in concentrations of 300-1000 cells per µl.

Single-cell sequencing and preprocessing of the sequencing data

A total of eight samples were sequenced; tissue-specific pooled samples from obese and non-obese atherosclerosis states, stained with the TotalSeq-C panel. The sequencing libraries

for gene expression and cell surface proteins were prepared used the 10X Genomics Chromium Next GEM Single Cell 5' Reagent Kits v2 Dual Index protocol, following manufacturer's instructions (CG000330 Rev A; kits PN-1000263, PN-1000190, PN-1000256, PN-1000215). In brief, approximately 17,000 cells from each sample were loaded onto Chromium Single Cell K chips, aiming to capture 10,000 single cells per sample. Single cells were partitioned into gel bead emulsions using a Chromium Controller (10x Genomics). After reverse transcription and cDNA barcoding, the emulsions were reversed and the subsequent steps were performed in bulk. Full-length cDNA was amplified with PCR (14 cycles) using a Veriti cycler (Applied Biosystems / Thermo Fisher). The libraries for the cell surface protein antibodies were prepared from unfragmented molecules. The libraries were finally indexed and amplified by PCR (14 cycles for gene expression libraries and 8 cycles for the cell surface protein libraries). The quality controls throughout the process were done with a Bioanalyzer 2100 (Agilent Technologies, US). The sequencing was done at Novogene using NovaSeq6000 with S4 flow cell. The reads were paired-end 150 bp. The data were preprocessed using 10X Genomics Cell Ranger V6 multi in a CSC - IT Center for Science (Finland) high performance computing (HPC) system with the configuration files in Figshare 10.6084/m9.figshare.29312825.

Quality control and sample integration

The single-cell analyses were run in R[14]. All scripts used for the following analysis workflows are available from https://github.com/BioTechnoAlchemist/TERVA. The initial quality controls and normalization of individual sample data were run in R (v4.1.2) on a local computer (MacOS Catalina 10.15.5), but the subsequent integrated analyses were run on a CSC HPC interactive environment with R (v4.2.1), under the Red Hat Enterprise Linux 8. Our analysis workflow started with quality control processes: first ambient RNA removal with SoupX v1.5.2[15], followed by crude pruning of the data in Seurat v4.1.1[16], and ultimately doublet removal with DoubletFinder v2.0.3[17].

Cell-free RNA or "ambient RNA" is a common source of noise in scRNAseq data and therefore a step to remove this noise was incorporated into the quality control workflow. We used either an automated estimation of ambient RNA or if that seemed too lenient (ambient RNA estimated to be less than 2 %), a reference list of genes (*Igkc*, *Ighg1*, *Ighm*, *Iglc2*, *Iglc3*, *Iglc1*, *Ighe*, *Ighg3*, *Ighd*) was used to estimate the global contamination fraction.

Droplet-based snRNAseq data may contain empty droplets and/or multiplets, so to remove clear outliers a crude pruning of the data was done by setting thresholds where the number of features for a cell must be between 200 and 5000. In addition, it was determined that the mitochondrial content of a cell must be less than 5-10 % to pass the quality control (depending on the sample, which was evaluated visually from violin plot before and after applying different thresholds). After the pruning, a basic Seurat data pipeline was run with default parameters to normalize and scale the data, after which DoubletFinder was used to find and remove possible remaining multiplets based on the expected multiplet rate dependent of the cells loaded reported by 10X Genomics in the CG000330 Rev A manual.

After the quality control steps were done on each sample, the data was transferred to the CSC Puhti server, where it was merged. At this point genes *Gm42418* and *AY036118* were removed from the data as they are commonly causing technical noise[18], after which the data

was renormalized and - scaled with the default parameters, followed by finding variable features using the "vst" method and number of the top variable features set to 3000, and principal component analysis (PCA) with the default parameters. Twenty first PC's were chosen based on an elbow plot of the proportion of variance explained by the PC's. Then uniform manifold approximation and projection (UMAP) dimensional reduction was run based on the PCA with 1:20 dimensions, followed by finding k-nearest neighbors (also using 1:20 dimensions), and finding clusters with resolution 0.6. The RunUMAP and RunPCA functions have a seed set to 42 by default and the same seed was used for the FindClusters function. The UMAP visualization of the merged data was inspected before data integration (Supplementary Fig 1). At this point one antibody was removed from the CITE-seq data because BioLegend reported a quality issue and mistaken identity in one antibody (Cd11a; correctly Cd28, clone 37.51), after which the CITE-seq data was also normalized using the centered log-ratio method. Moreover, because CITE-seq data may suffer from major background noise, to address this issue, we leveraged "dsb" (denoised and scaled by background) R package to normalize and denoise the protein expression data[19]. We defined the cell protein matrix and empty droplet matrix using the raw data produced by the CellRanger. To normalize the protein expression data, "DSBNormalizeProtein" function was used with "denoise.counts" and "use.isotype.control" parameters set to "TRUE". "IgG1_kappa_isotypeCtrl", "IgG2a_kappa_isotypeCtrl", and "IgG2b_unknown_isotypeCtrl" were used as isotype controls. Each sample was processed separately and then integrated.

Next, the data was integrated with Harmony [20] using "sample" as the variable to integrate out. Then the UMAP dimensional reduction technique was rerun with the harmony embeddings using the first twenty embeddings. Finding nearest neighbors and UMAP were also rerun with the same first twenty harmony embeddings. Then finding clusters was rerun with resolutions from 0 to 1.5 with 0.1 increments and Clustree-package (v0.5.0,[21]) was utilized to visually inspect an appropriate clustering resolution (Supplementary Fig 2), which was evaluated to be 0.7. While visually inspecting some major immune cell markers with the FeaturePlot function, we found a cell population that was double positive for *Cd79a* and *Cd3d* genes (Supplementary Fig 3). Closer inspection of RNA expression in these cells showed that 1292/1555 (83.09 %) of the cells were concurrently positive for multiple B and T cell specific markers *Cd79a*, *Cd19*, *Cd3d*, *Cd3e* and *Cd3g*, and and 1380/1555 (88.75 %) were double-positive for the Cd19 and Cd3 proteins in the CITE-seq data. The majority of these multipositive cells were from the aorta samples (1374/1555 cells; 977 cells from the non-obese and 397 cells from the obese-derived samples) and because we could not exclude the possibility of technical causes for the multipositivity from the sample preparation and processing, this cluster was removed from the subsequent analyses, reducing the total cell count from 47495 to 45940.

Cell annotation and differential gene expression analysis

Cell types were defined by combining automated (SingleR v1.6.1 and celldex v1.6.0 packages [22]) and manual cell annotation aided by the CITE-seq data. We used MouseRNAseqData from celldex to create the reference for the automated annotation[23]. The subsequent differential gene expression analyses (between clusters and between atherosclerosis

states in different cell types within tissues) were run with Wilcoxon rank sum test. Threshold for significance was adjusted P-value < 0.05.

Gene set enrichment analysis

Gene set enrichment analyses (GSEA) using GO, KEGG and Reactome databases were carried out with g:Profiler [24] (version *e110_eg57_p18_4e6dcbc3*) using their web interface at https://biit.cs.ut.ee/gprofiler/gost. The visualization was carried out on the g:profiler generated output files using the R-packages multienrichjam (0.0.82.900), enrichplot (v1.23.1.992) in a local environment (macOS Monterey 12.6.7, R-version 4.3.3). We used our own R-script to mine immune-related terms and pathways from the g:profiler output csv-files. The words used in this analysis were ("immune", "immunity", "inflammation", "inflammatory", "mhc", "complement", "c1", "c2", "c3", "c4", "hypersensitivity", "autoimmune", "leukocyte", "defense", "cytokine", "interferon", "interleukin", "antigen", "neutrophil", "granulocyte", "platelet", "macrophage", "th1", "th2", "th17", "dendritic cell", "t cell", "b cell", "rheuma", "arthritis", "atherosclerosis", "lupus", "diabetes", "viral", "bacterial", "graft").

Trajectory analysis

The trajectory analyses were run with the R-package Totem (v0.99.2)[25], which uses SingleCellExperiment-objects. The conversion from seurat-object to a SingleCellExperiment-object was done with the SingleCellExperiment R-package (v1.18.0) and required dimensional reduction was carried out with the dyndimred R-package (v.1.0.4).

Single-cell regulatory network inference and clustering (SCENIC) analysis

We employed the pySCENIC (v0.12.1) Python package to infer transcription factors (TFs) within various fibroblast subpopulations[26]. Initially, we utilized GRNBoost2 to analyze Gene Regulatory Networks (GRNs) based on the co-expression patterns of TFs and their target genes. Next, we applied the cisTarget function to identify putative regulatory regions of the target genes. This function enabled the identification of enriched TFs within each module, where a module is defined as a TF and its potential target genes. The relative biological activity of the identified modules in individual cells was quantified using the AUCell function. Regulon Specificity Scores (RSS) were calculated using the Jensen–Shannon Divergence[27] to evaluate the cell-type specificity of the modules.

Cell interaction analysis

Network analyses were executed with the NicheNet package v1.1.1[28] in the CSC Puhti HPC environment. The required network and ligand-target matrix input files for the basic seurat-based NicheNet-pipeline were downloaded from https://zenodo.org/record/3260758.

The sender cell types were: B cells, *Mfap4+* fibroblasts, *Ccl11+* fibroblasts, *Mgp+* activated fibroblasts, *Lef1+ Tcf7+ Cd4+* T cells, *Gpihbp1+ Fabp4+* endothelial cells, classical and non-classical monocytes, conventional dendritic cells, *Folr2+ Lyve1+* M2 macrophages, *Ccl4+ Cxcl2+ Ccl3+* inflammatory macrophages, *Pf4+ Retnla+* macrophages, mesothelial cells, *Fscn1+ Apol7c+* dendritic cells, intermediate monocytes, NK cells, plasma cells, *s100a9+/a8+* granulocytes, and VSMCs.

Sample collection of human carotid arteries and aorta for spatial transcriptomics

A sample of atherosclerotic aorta was obtained from a 67-year-old male undergoing aorto-femoral bypass surgery due to chronic, symptomatic peripheral artery disease. Carotid artery plaque samples were obtained from a 61-year-old female and a 60-year-old male undergoing surgical endarterectomy due to critical carotid artery stenosis, with symptom onset less than two weeks. The study conforms to the Declaration of Helsinki, the institutional review boards of the Hospital District of Southwest Finland and Turku University Hospital approved the study (permit number T03/024/19, ethical statement number T75_2011), and patients gave written informed consent.

Histological and immunofluorescence staining of human aorta and carotid artery sections

The tissues were embedded in optimal cutting temperature compound, frozen at −70°C, and cut into 6 µm cryosections and stained with hematoxylin-eosin (H&E). The stained slides were scanned with a digital slide scanner (Pannoramic 1000 Flash; 3DHISTECH, Ltd., Budapest, Hungary). To examine the expression of CD68, Mannose receptor and Folate receptor-beta (FR-β; alias CD206) positive macrophages on the lesion region of the tissues. Subsequent adjacent sections were formalin fixed for 10 minutes then treated with epitope retrieval solution pH 6, Leica RE7113, followed by blocking with Normal antibody diluent (BD09-125, WellMed BV, Duiven, The Netherlands). These sections were double stained with mouse anti-human CD68 (1: 1000; catalog number: M0876, Dako Agilent, city, country) and rabbit polyclonal anti-Mannose receptor antibody (1: 1000; catalog number: ab64693, Abcam, Cambridge, United Kingdom) followed by goat anti-Mouse Alexa Fluor 488 conjugated secondary antibody (1:1000; catalog number: A-11017, Invitrogen, ThermoFisher Scientific, Waltham, United States) and donkey anti-rabbit Alexa 549 (1:1000; catalog number: A21207, Invitrogen, ThermoFisher Scientific, Waltham, United States) or anti-human CD68 and anti-human FR-β allophycocyanin (APC)-conjugated antibody (1:100, mouse IgG2a; BioLegend, San Diego, CA, United States) followed by goat anti-Mouse Alexa Fluor 488 conjugated secondary antibody (1:1000; catalog number: A-11017, Invitrogen, ThermoFisher Scientific). Then the sections were mounted with ProLong Gold antifade with DAPI (catalog number: P36931, Invitrogen, ThermoFisher Scientific, Waltham, United States). The stained slides were finally scanned with a digital slide scanner (Pannoramic Midi fluorescence slide scanner; 3DHISTECH, Ltd., Budapest, Hungary), then images were made using Caseviewer software (3DHISTECH, Ltd., Budapest, Hungary). The H&E and IF staining were used to select the regions of interest for the spatial transcriptomics experiment (Supplementary Fig 4).

Spatial transcriptomics sample processing and sequencing

A spatial transcriptomics experiment was carried out on human aorta and carotid artery sections using the 10X Genomics Visium (V1) gene expression platform. Of each sample, two technical replicates were generated from adjacent sections. Therefore, we carried out the spatial transcriptomics on a total of eight sections. The imaging required for the protocol was carried out by the researchers at the Cell Imaging and Cytometry core facility using a Nikon Eclipse

Ti2-E microscope equipped with a Nikon DS-Fi3 CMOS camera with the specifications explained in the CG000241 Visium Imaging Guidelines Rev B. RNA integrity number (RIN) was determined for the samples with the Bioanalyzer 2100 and Eukaryote Total RNA 6000 Pico kit (5067-1513, Agilent). The carotid arteries had RIN values of 6.10 and 7.70, and the aorta sample had a RIN value of 6.90. Optimal permeabilization time was determined from carotid samples and due to similar tissue structure, the same permeabilization time (18 minutes) was used for the aorta and carotid arteries. The protocols used were: Demonstrated Protocol Methanol Fixation and HE Staining CG000160 Rev C, Visium Spatial Tissue Optimization User Guide CG000238 Rev D, and Demonstrated Protocol Visium Spatial Protocols Tissue Preparation Guide CG000240 Rev D.

The sequencing libraries were constructed following the Visium Spatial Gene Expression User Guide CG000239 Rev F and cDNA and subsequent library quality was checked with the Bioanalyzer 2100 using the High Sensitivity DNA Assay (5067-4626, Agilent). The sequencing was carried out with Illumina NovaSeq using an SP flow cell with the recommended 28+10+10+90 bp read lengths, by the Finnish Functional Genomics Centre, and they used Space Ranger (v1.3.1) to generate the count matrices for downstream analyses. Space Ranger raised a low fraction reads in spots warning for the sections of the first region of the aorta samples, which may be a result of nonoptimal permeabilization. The other two aorta (second region) and four carotid artery sections had no flags. Subsequent QC was carried out separately for each section in Seurat (v5.3.0) in R (v4.4.1) in a local environment using an MacOS Sequoia v15.4.1 system. Low quality spots were filtered with variable threshold for number of genes per spot per section (40-90 for aorta and 60-100 for carotid artery samples). The thresholds for the mitochondrial and ribosomal gene content were 15 and 20 percent for each section, respectively. Before gene mapping, data log-normalization, scaling, and finding of variable features were carried out similar to the single-cell workflow.

Immunohistochemistry and multiplexed immunofluorescence staining of mouse tissues

IHC and multiplex-IF experiments were carried out on horizontal sections of the ten individual AO-PVAT samples. The paraffin embedding and subsequent IHC/mIF stainings of the sections were carried out at the Histology core facility of the Institute of Biomedicine, University of Turku, Finland. For routine IHC, each experiment slide had a total of five stained sections so that each slide contained either two early disease and three late disease samples or vice versa.

For routine IHC, antigen retrieval for PI16 and CD74 was performed with a pressure cooker (Decloaking chamber NxGen, Biocare Medical) for 20 minutes using citrate buffer with pH 6.0 (BioSite, BSC-OKHURL) and for CD19 with a microwave (7 minutes 600 W + 7 min 450 W + 20 minutes of cooling down) with Tris-EDTA buffer with pH 9.0 (BioSite, BSC-2OIB1M). Staining was done with a semiautomated Labvision autostainer (Thermo Fisher Scientific). Washing buffer was 0.05 M Tris-HCL with pH 7.6 (Reagena, 112270) and 0.05 % Tween 20 as a detergent. Blocking was carried out with hydrogen peroxide and Normal antibody diluent (BD09, Immunologic) or Dako REAL antibody diluent (S2022, Agilent) (see * in Supplementary Table 1) in room temperature (RT). The primary and secondary antibodies are listed in Supplementary Table 1. PI16, CD74, and CD19 primary antibodies were incubated

for 60 minutes in RT, followed by secondary antibody incubation for 30 minutes. BrightDAB substrate (WellMed, BS04-110) was used with 10-minute incubation, followed by counter staining with Mayer's hematoxylin (1 minute in RT).

Multiplex-IF was performed by using Leica BOND RX automated stainer (Leica Biosystems). After 30 minutes of baking at 60°C and paraffin removal (Leica BOND Dewax Solution, AR9222, Leica Biosystems), slides were heated for 20 minutes at 100°C in antigen retrieval solution (Leica BOND Epitope Retrieval Solution 2, AR940, Leica Biosystems) and blocked for endogenous peroxidases in 3% hydrogen peroxide for 10 minutes at RT. Total of four staining rounds were carried out as follows: Protein blocking by Normal antibody diluent (10 minutes at RT) or Dako REAL antibody diluent (for PI16), primary antibody incubation (20 minutes at RT, Supplementary Table 1), secondary antibody incubation (10 minutes at RT, Supplementary Table 1), tyramide signal amplification by incubating slides with corresponding fluorophore-conjugated tyramide (Supplementary Table 1) for 10 minutes in 2 nM final concentration in Tyramide Amplification Buffer Plus (15129, Biotium), supplemented with fresh 0.0015% hydrogen peroxide. Antibodies were removed by heating slides for 10 minutes at 98°C in antigen retrieval solution (Leica BOND Epitope Retrieval Solution 2) and the whole staining cycle was repeated for each marker in the following order: PI16, F4/80, CD4, CD3. Slides were washed with Bond Wash Solution (AR9590, Leica Biosystems) in between steps and mounted with ProLong Gold Antifade Mountant with DAPI (P36935, Thermo Fisher Scientific). As negative control for F4/80, CD3e and CD4, rabbit IgG isotype control was used instead of primary antibody (Normal antibody diluent for PI16 as negative control). Imaging of the mIF-stained tissues was done with Leica Thunder widefield fluorescence microscope at the Cell Imaging and Cytometry core facility, at Turku Bioscience Centre.

Tissue imaging and image analyses (PI16+ cell counts and morphometric analysis)

Imaging of all mouse tissues was carried out by the researchers at the Cell Imaging and Cytometry core facility using a Nikon Eclipse Ti2-E microscope equipped with a Nikon DS-Fi3 CMOS camera and/or Pannoramic P1000 slide scanner (3DHISTECH, Budapest, Hungary). Image annotations for the subsequent image analysis were done with QuPath[29]. The images and metadata used for the different analyses are available (see Data availability).

The morphometric analysis was carried out at the Medisiina Imaging Centre, University of Turku. The quantitative analysis of the scanned histological sections was performed using Visiopharm software version 2022.07 (Horsholm, Denmark). First, adipose tissue areas were labelled by a deep learning classifier, and the predicted labels were corrected manually where necessary. Adipose cells were then labelled using a workflow adapted from Iron Hematoxylin, Adipose Tissue analysis protocol package (#10113, visiopharm.com/app-center). Parameters of the original analysis protocol package were adjusted to optimize the correct detection of the adipose cells in the current tissues and staining. Areas of labelled adipose cells were extracted as the output. The data acquired from the previous steps was then analysed locally using a MacOS Sequoia v15.4.1 with the R (v4.4.1) base package stats, dplyr (v1.1.4) and visualized with ggplot2 (v3.5.2). The normality of the data was assessed using Shapiro-Wilk test, and after determining that the data is drawn from a normal distribution, we decided to use a one-way (two-sample) Welch t-test.

For counting of the PI16+ fibroblasts, we used the nucleus detection method from[30] and fine-tuned it for IHC staining data by applying domain adaptations (DA) in two steps. For the first DA step, positive detections were used as pseudo labels (both detection thresholds set to 0.4) and 1000 detections were randomly chosen for re-training the network (5 epochs). Second DA step was then performed using detections by the network from previous training round (thresholds 0.6 and 0.2), this time 10000 randomly selected detections were used for training (50 epochs). The resulting network was then used for nucleus detection form regions of interest. Positively stained cells were defined by thresholding (0.2) the brown channel of detected nuclei locations.

The following statistical analysis to compare estimated mean cell counts of obese and non-obese groups was carried out locally (as described above) in R. First, to examine the group differences we fit a generalized linear model using beta distribution with glmmTMB- package (v1.1.11)[31], which is an appropriate strategy for analysing proportions that can only vary between 0-1. Then we evaluated the model fit using DHARMa (v0.4.7)[32]. To compare the estimates from the generalized linear model, a Type III Anova test was done with the car-package (v3.1-3)[33]. Finally, we used emmeans-package (v1.11.1)[34] to generate the estimated marginal means, which were used to inspect how the estimated group means diverged. The emmeans-package was also used to visualize the results.

Results

Tissue-specific characterization of the cellular landscape in murine model of atherosclerosis

Using 5' single-cell RNA sequencing combined with partial CD45+ enrichment and CITE-seq (Fig 1A), we generated a data of ~46000 cells. The unsupervised clustering of the integrated data which included all the tissues and both obesity states identified 40 clusters. Using a combination of automated and manual cell annotation, we defined 13 major cell types that corresponded to a total of 32 different cell states and were clearly present in both model states (Fig 1B and C). These included five different T cell populations (T memory cells, *Cd8*+ and *Cd4*+ T cells positive for *Lef1* and *Tcf7*, *Cd8*+ cytotoxic T cells, and regulatory T cells), five fibroblast (*Pi16*+, *Ccl11*+, *Mfap*+, *Mgp*+, and *Il1b*+) subpopulations, four macrophage populations (M2, M1, *Trem2*+ foamy, and *Pf4*+ *Retnla*+ macrophages), three vascular smooth muscle cell (VSMC) populations, two B cell (B cells and plasma cells), two dendritic cell (conventional and *Fscn1*+ *Apol7c*+ DC), two endothelial cell, two monocyte (intermediate and classical and non-classical as one), one granulocyte, one innate lymphoid cell (ILC), one natural killer (NK), one mast cell, and one mesothelial cell population. Moreover, one mixed *Mki67*+ *Top2*a+ proliferating population, and a separate small cluster demonstrating high expression of both endothelial and fibroblast markers (*Pecam1*, *Cdh5*, *Col1a1*, and *Lum*). The top five most abundant cell types per tissue and obesity state are shown in Table 1.

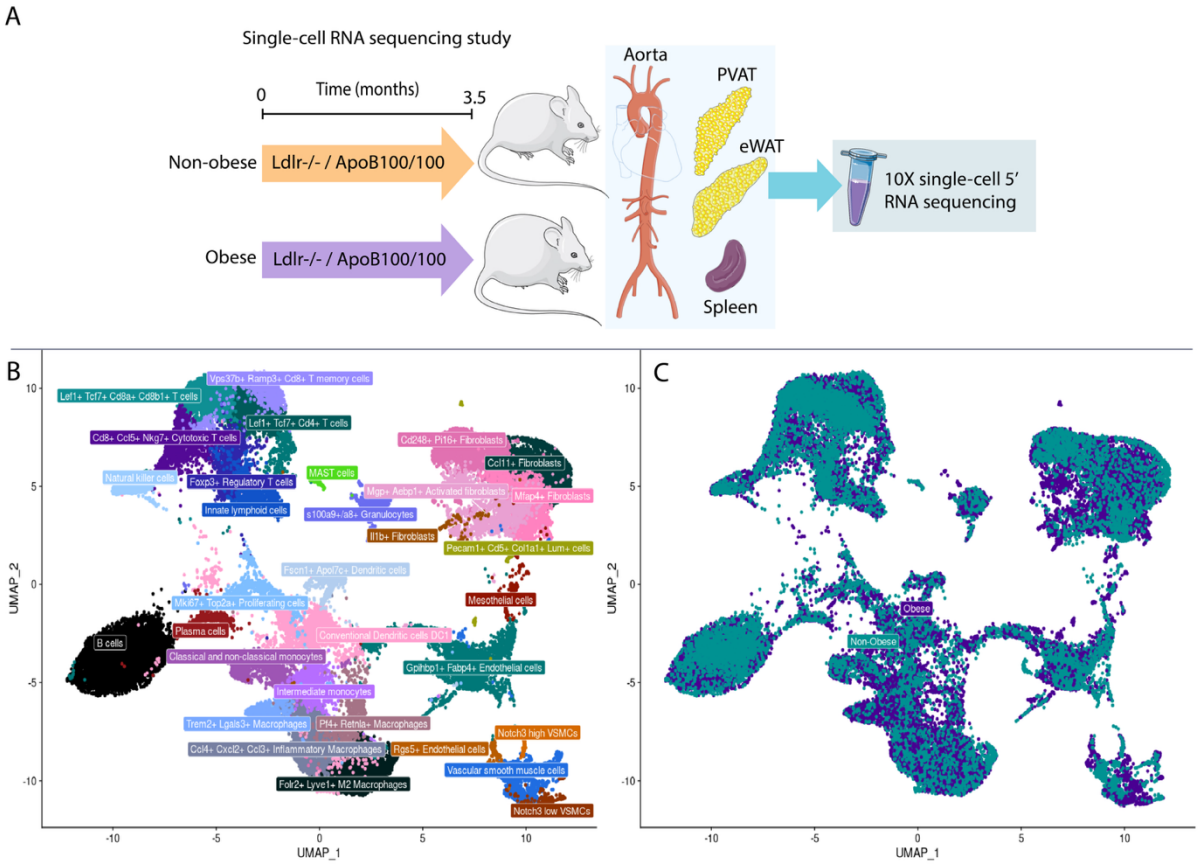

Figure 1. Study design, cell type annotations, and obese/non-obese status of cells. A) Study design of the single-cell RNA sequencing study (Image created using Servier Medical Art, licensed under CC BY 4.0), B) UMAP projection of the integrated data with cell type

annotations, and C) UMAP projection of the integrated data showing the obesity status of each cell.

The cells from the aortas were CD45-enriched and the observed cell types were biased towards different immune cell populations (Table 1). Surprisingly, the most abundant cell type in aorta and PVAT were B cells, which was not expected based on literature, and we hypothesized that lymph node-derived B cell contamination was likely impacting these cell counts. To confirm this, we carried out a CD19 IHC staining in the validation set of PVAT-aorta tissue sections and the marker was detected in the lymph nodes and lymph vessels but not elsewhere in the PVAT or aorta (Supplementary Fig 5).

Table 1. Top five most abundant cell types in obese and non-obese samples per tissue.

Tissue	Cell type in obese mice	Proportion of the total cell count in the sample	Cell type in non-obese mice	Proportion of the total cell count in the sample
Aorta	B cells	23.2 (614/2651)	B cells	24.7 (1652/6684)
	VSMC	8.4 (223/2651)	Conventional Dendritic cells DC1	8.9 (594/6684)
	Vps37b+ Ramp3+ Cd8+ T memory cells	7.7 (203/2651)	*Ccl4+ Cxcl2+ Ccl3+* Inflammatory Macrophages	8.7 (584/6684)
	Ccl4+ Cxcl2+ Ccl3+ Inflammatory Macrophages	7.6 (201/2651)	*Vps37b+ Ramp3+ Cd8+* T memory cells	8.6 (575/6684)
	Trem2+ Lgals3+ Macrophages	7.1 (187/2651)	*Folr2+ Lyve1+* M2 Macrophages	8.1 (542/6684)
eWAT	*Gpihbp1+ Fabp4+* Endothelial cells	16.5 (1314/7986)	*Gpihbp1+ Fabp4+* Endothelial cells	19.3 (1238/6411)
	Folr2+ Lyve1+ M2 Macrophages	14.4 (1152/7986)	*Folr2+ Lyve1+* M2 Macrophages	15.1 (970/6411)
	Ccl11+ Fibroblasts	13.1 (1043/7986)	*Ccl11+* Fibroblasts	10.4 (668/6411)
	Ccl4+ Cxcl2+ Ccl3+ Inflammatory Macrophages	6.6 (530/7986)	*Cd248+ Pi16+* Fibroblasts	7.5 (482/6411)
	Cd248+ Pi16+ Fibroblasts	6.0 (478/7986)	*Ccl4+ Cxcl2+ Ccl3+* Inflammatory Macrophages	7.4 (477/6411)
PVAT	*Mgp+ Aebp1+* Activated fibroblasts	11.5 (843/7343)	B cells	19.5 (1050/5377)
	Mfap4+ Fibroblasts	11.4 (835/7343)	*Cd248+ Pi16+* Fibroblasts	11.6 (623/5377)

	Cd248+ Pi16+ Fibroblasts	8.6 (632/7343)	*Ccl11+* Fibroblasts	7.7 (412/5377)
	Ccl11+ Fibroblasts	8.4 (618/7343)	*Mfap4+* Fibroblasts	7.2 (385/5377)
	Gpihbp1+ Fabp4+ Endothelial cells	6.7 (492/7343)	Classical and non-classical monocytes	6.1 (328/5377)
Spleen	B cells	20.6 (869/4228)	B cells	26.4 (1387/5260)
	Lef1+ Tcf7+ Cd4+ T cells	20.5 (868/4228)	*Lef1+ Tcf7+ Cd4+* T cells	21.1 (1108/5260)
	Lef1+ Tcf7+ Cd8a+ Cd8b1+ T cells	18.2 (769/4228)	*Lef1+ Tcf7+ Cd8a+ Cd8b1+* T cells	19.8 (1040/5260)
	Foxp3+ Regulatory T cells	9.7 (411/4228)	*Foxp3+* Regulatory T cells	9.2 (485/5260)
	Cd8+ Ccl5+ Nkg7+ Cytotoxic T cells	8.7 (366/4228)	*Cd8+ Ccl5+ Nkg7+* Cytotoxic T cells	7.8 (410/5260)

Differential gene expression analysis highlights Cd74 and Apoe as key genes between the obesity states in multiple cell types across tissues

To reveal potential disease driving genes we carried out differential gene expression analyses between the obese and non-obese atherosclerosis states in the key cell types. Below we describe the changes within the tissues in the cell populations where at least one gene was showing Log2 Fold change (Log2FC) greater than 1.5 (full lists of DE genes are provided in Supplementary Tables 2-4).

The most prominent changes were observed in the two adipose tissues, PVAT and eWAT (Fig 2 A-G). In spleen none of the observed gene expression changes reached the set Log2FC threshold, while in aorta, the changes were generally of smaller effect and were restricted to *Cd8+* Tmem cells and *Fscn1+ Apol7c+* DC populations (Fig 2 H-I). Moreover, we unexpectedly observed many immunoglobulin variable genes and Joining Chain Of Multimeric IgA And IgM (*Jchain*) among the most upregulated genes in these aorta-derived cells. We highly suspect that the presence of these transcripts was a technical artefact. Unlike the other tissue types, the aortas were enriched for CD45+ cells before pooling, which could have introduced more debris (see Methods). The removal of ambient RNA, even when focusing on these immunoglobulin transcripts specifically, as recommended in[15] where a similar phenomenon was observed, did not resolve the issue. To avoid skewing the results by removing these transcripts, we concentrated on the other upregulated genes instead. The most highly upregulated gene in the aorta-derived T memory cells was *Cd74* (CD74 Molecule, also known as HLA-DR antigens-associated invariant chain; Log2FC ~1.8, Supplementary Table 2), which was also observed upregulated in other cell types. Some histocompatibility 2 antigens (*H2-Aa* and *H2-Eb1*) were also upregulated, but their Log2FCs were less than 0.9 (Supplementary Table 2). In the DC population the most upregulated genes, excluding the immunoglobulin variants, were *Cxcl2* (C-X-C Motif Chemokine Ligand 2, Log2FC ~ 1.5), and *Apoe* (Apolipoprotein E, Log2FC ~ 1.1) (Supplementary Table 2).

The two adipose tissues showed more marked changes. In PVAT, for instance, four different cell populations demonstrated notable changes between the two atherosclerosis model states: activated (*Mgp*+) fibroblasts and *Pi16*+ progenitor fibroblasts, one EC population, and intermediate monocytes (Fig 2 A-D). The highest Log2FCs in the activated fibroblasts were observed for *Cd74*, *Lyz2* (~ 2.3-3.5, Supplementary Table 3), and three Histocompatibility 2, class II antigens (*H2-Eb1*, *H2-Ab1*, and *H2-Aa,* Log2FC ~ 2.3-2.5). *Lyz2* and *Cd74* were also highly upregulated (Log2FC ~ 2.3-2.4) in the *Pi16*+ progenitor fibroblasts, while the other top genes were *Apoe* (Log2FC ~ 2.6, and the complement chain encoding genes *C1qb*, and *C1qa* (Log2FC ~ 2.1, Supplementary Table 3). In the ECs, *Cd74* was observed once again with a Log2FC of ~ 2.1, while some of the other highly expressed genes during obesity were *Gsn* (Gelsolin, Log2FC ~ 2.3) and the same histocompatibility antigens as in the activated fibroblasts (H *H2-Aa, 2-Eb1*, and *H2-Ab1*, with Log2FC of ~ 2.0, ~ 1.9, and ~ 1.7, respectively). Finally, in the intermediate monocytes, the four most upregulated genes in obesity were *Ly6e* (Lymphocyte Antigen 6 Family Member E, Log2FC ~ 2.9), *Plac8* (Placenta Associated 8, Log2FC ~ 2.9), *Ly6c2* (Lymphocyte Antigen 6 Family Member G6C, Log2FC ~ 2.4), and *Apoe* (Log2FC ~ 1.9).

In eWAT the most remarkable gene expression changes were observed in activated *Mgp*+ fibroblasts, *Trem2*+ macrophages, and VSMCs (Fig 2 E-G). The most upregulated genes in the activated *Mgp*+ fibroblasts were *Apoe* (Log2FC ~ 1.7), *C4b* (Complement component 4b; Log2FC ~ 1.5) (Supplementary Table 4). In the *Trem2*+ macrophages the most upregulated genes were *Gpnmb* (Glycoprotein Nmb; Log2FC ~ 1.6), and Mfge8 (Milk Fat Globule EGF And Factor V/VIII Domain Containing; Log2FC ~ 1.5) (Supplementary Table 4). Finally, the four of the most upregulated genes in VSMCs were *Acta2* (Actin Alpha 2, Smooth Muscle; Log2FC ~ 2.4), *Tagln* (Transgelin; Log2FC ~ 2.0), *Nrip2* (Nuclear Receptor Interacting Protein 2; Log2FC ~ 2.0), and *Mustn1* (Musculoskeletal, Embryonic Nuclear Protein 1; Log2FC ~ 1.8) (Supplementary Table 4).

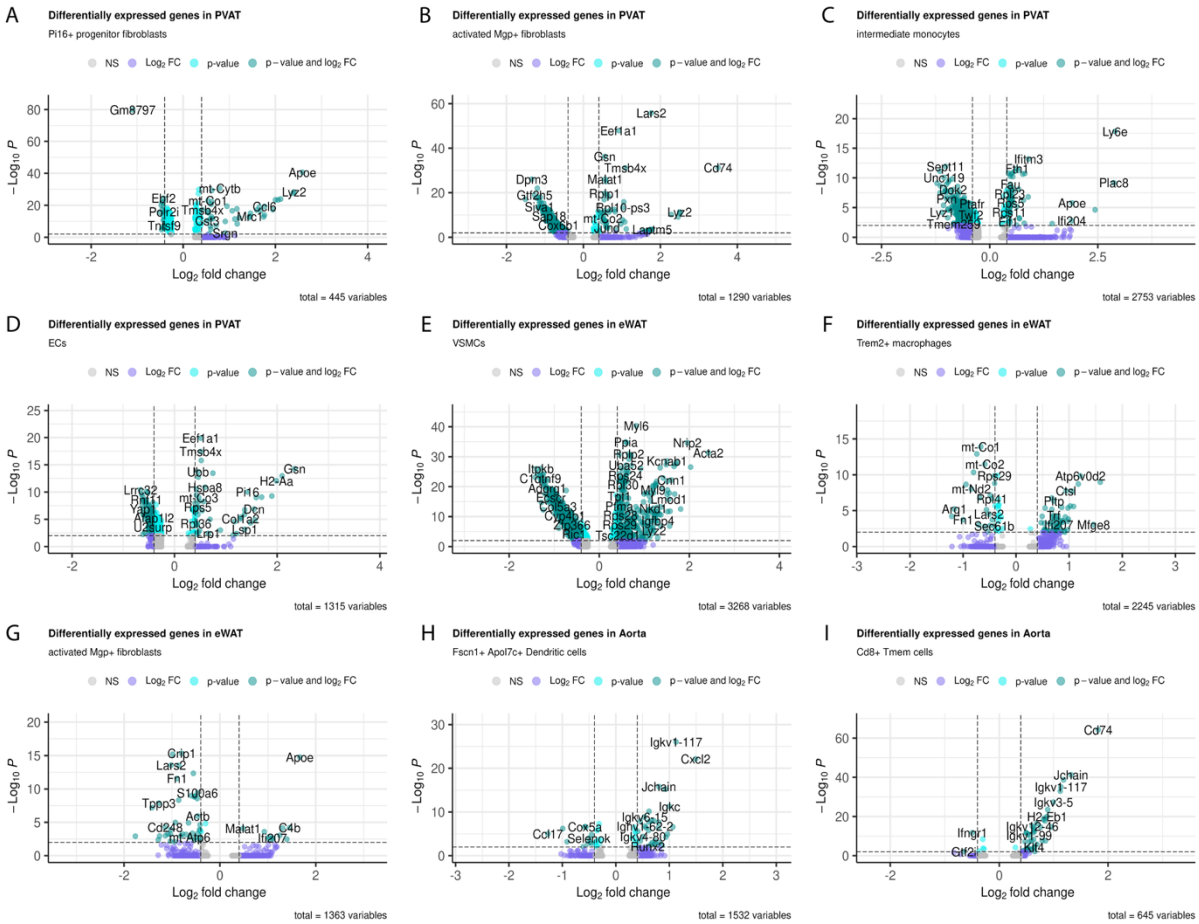

Figure 2. Differentially expressed genes between the obese and non-obese states in PVAT (A-D), eWAT (E-G), and aorta (H-I). Positive fold changes indicate higher expression in the obese state.

Gene set enrichment analysis highlights the upregulation of immune-related processes in PVAT-derived fibroblasts during obesity

As the different fibroblast subpopulations were recurring in the most highly affected cell types in the differential gene expression analyses, we focused our downstream analyses on them. Interrogation of gene lists ordered by the Log2FC from the DE analysis revealed a multitude of affected processes in the gene set enrichment analysis. The analysis was done for both up- and downregulated genes with g:Profiler[24], concentrating on the GO molecular functions and biological processes, and the KEGG and REACTOME pathway results. We also performed a text mining analysis to map any immune-related phrases. The top up- and downregulated terms, and the term's relationships to the DE genes are in Fig 3.

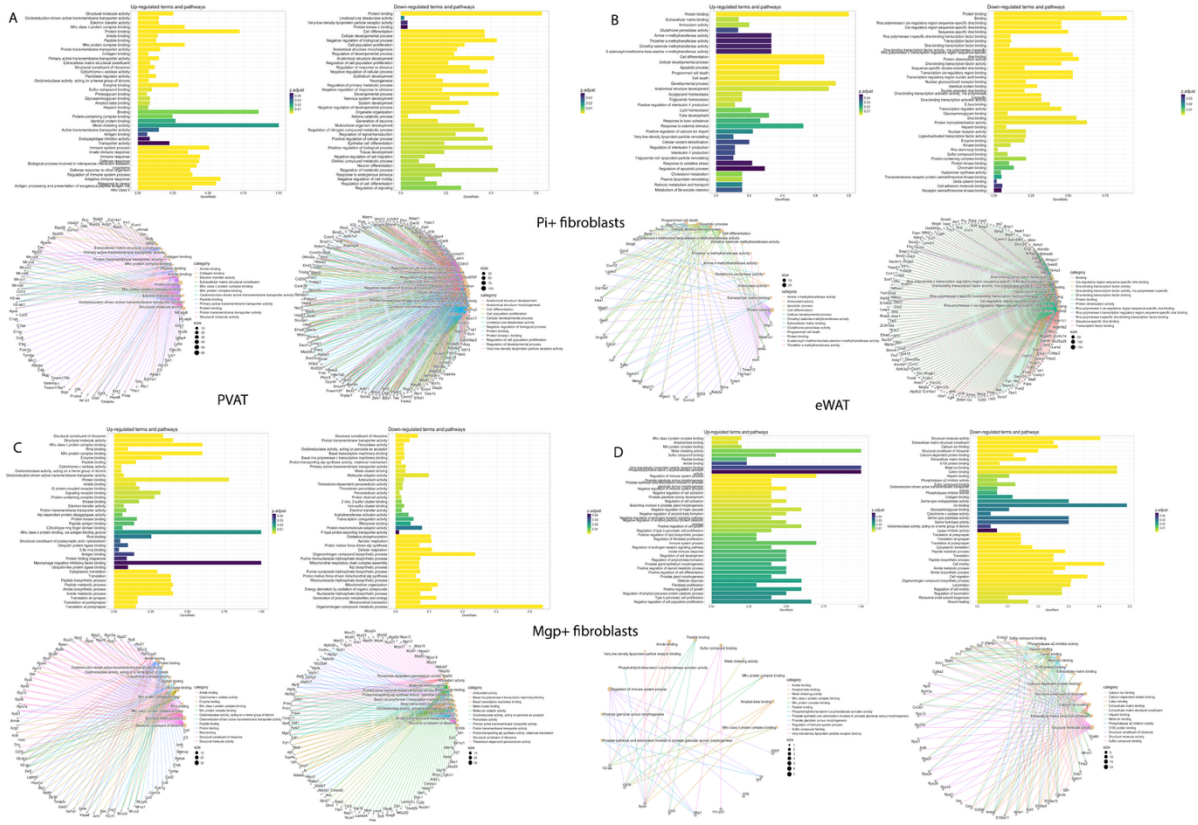

Figure 3. Top enriched terms based on the up- and downregulated DE genes (bar plots), and relationships of the terms with the DE genes (circular cnet plots): A) PVAT Pi16+ fibroblasts, B) eWAT Pi16+ fibroblasts, C) PVAT Mgp+ fibroblasts, and D) eWAT Mgp+ fibroblasts.

First, we investigated the PVAT-derived *Mgp+* and *Pi16+* fibroblasts, which exhibited strong differential gene expression between the obesity states. GSEA analysis of the upregulated DE genes in PVAT-derived *Pi16+* fibroblasts resulted in 301 hits (Supplementary Table 5). In total, ~35 % (105/301) phrases were found to be immune-related, indicating strong immune activation, including possible antigen presentation-related functions, in these fibroblasts during obesity. Meanwhile, the analysis of the downregulated genes revealed 82 affected GO terms (Supplementary Table 5). The only immune-related term was a GO Biological Process "Negative regulation of macrophage activation". In contrast, similar analysis of eWAT-derived *Pi16+* fibroblasts identified 34 hits among upregulated DE genes and 596 hits among downregulated genes (Supplementary Table 6). Only three upregulated terms were immune-related, all linking specifically to interleukin-1 production or its regulation, and the rest were linked to the homeostasis of triglycerides and lipid levels, and lipoprotein remodelling. Meanwhile, approximately 7% (40/588) of the downregulated GO terms were immune-related, reflecting decreased processes in eWAT-derived *Pi16+* fibroblasts during obesity, including leukocyte dynamics, T cell activation, and antigen/cytokine signalling. Interestingly, fat cell differentiation related functions were also downregulated (Supplementary Table 6). These results highlight that eWAT and PVAT-derived *Pi16+* fibroblasts have very different functions during obesity.

Next, looking at the *Mgp+* fibroblasts in PVAT, we observed 335 terms based on the upregulated DE genes (Supplementary Table 5). Again, immune-related terms and pathways

were highly emphasized to be upregulated; ~ 37 % (106/286) GO terms and ~ 43 % (12/28) of the KEGG pathways were related to immunity. Antigen processing and presentation, especially via the MHC class II pathways, were highly represented in the results, as was for *Pi16+* fibroblasts in the same adipose tissue. However, most fascinating enrichment of terms was the representation of autoimmune related KEGG pathways: allograft rejection, autoimmune thyroid disease, graft-versus-host disease, rheumatoid arthritis, systemic lupus erythematosus and Type I diabetes mellitus. The GSE-analysis results based on the downregulated DE genes in *Mgp+* fibroblasts in PVAT did not include anything immune-related but instead were focused on e.g. thermogenesis, cellular oxidative processes and respiration, and detoxification and responses to oxidative stress (Supplementary Table 5). In eWAT, the *Mgp+* activated fibroblasts also had upregulated immune-related functions during obesity (Fig 3), while processes such as structural molecule activity, ECM structural constituents and ECM binding as well as cell migration, motility and locomotion functions were downregulated (Supplementary Table 6). This indicates that the *Mgp+* fibroblasts are more similar between the adipose tissues in comparison with the *Pi16+* fibroblasts which clearly demonstrated very divergent functions between PVAT and eWAT.

Spatial transcriptomics mapping of mouse model gene signatures onto human arterial tissues

To examine how the top differentially expressed genes from our mouse model are expressed in human tissues, we carried out a spatial transcriptomics experiment using 10X Genomics Visium V1 platform. Data generated from human aorta and carotid artery samples acquired from three different endarterectomy patients were analysed with the R-package Seurat. After basic quality control, we mapped the key genes of interest, which were indicated in our single-cell analysis as being differentially expressed between the mouse model obesity states (Fig 4). We observed that some of the genes derived from the mouse data were highly expressed both in human aorta and carotid arteries (e.g. *CD74*, *APOE*, *MGP*, and *HLA-DRB1*). On the other hand, *JCHAIN* was strongly expressed in aorta but much less in carotid arteries and seemed to have an inverse spatial relationship with APOE expression, but evident spatial co-expression with several immunoglobulin genes (Fig 4 A and D), which could imply plasma cell activity in those regions. *PI16* expression was negligible in all samples, which was to be expected because they strictly contained the aortic or carotid artery wall and no adventitia or other surrounding tissues.

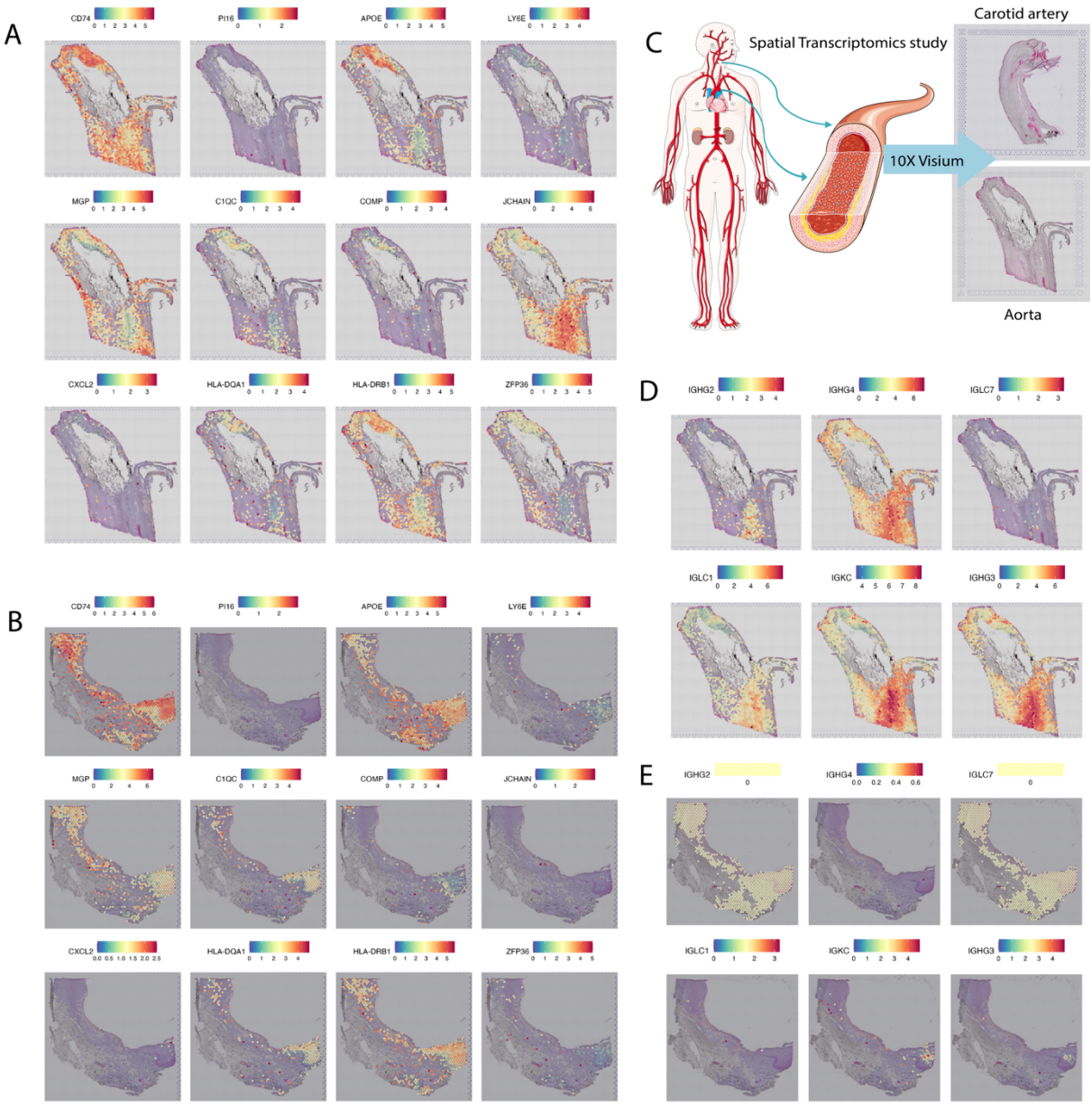

Figure 4. Expression of selected DE genes from the mouse model on human arterial tissues (genes: CD74, PI16, APOE, LY6E, MGP, C1QC, COMP, JCHAIN, CXCL2, HLA-DQA1, HLA-DRB1, ZFP36). A) Genes of interest (from single cell study) in human aorta, B) genes of interest in human carotid artery, C) Study design, D) Immunoglobulin expression in aorta, E) immunoglobulin expression in carotid artery.

PI16+ fibroblasts are found in aortic adventitia, plaques and within the PVAT, and their numbers are reduces in obese state.

To confirm the localization of the *Pi16+* progenitor fibroblasts in target tissues, we used immunohistochemistry of PI16 on sections from formalin-fixed paraffin-embedded (FFPE) tissues from ten individual mice representing the two disease model states. The PI16 expression was clearly localized in the fibroblasts in specific patterns (Fig 5) around the adipose tissue in the PVAT and the adventitia of the aorta as expected from a previous study[35]. Although the

patterning was observed in both disease model states, there were differences between the non-obese and obese mice.

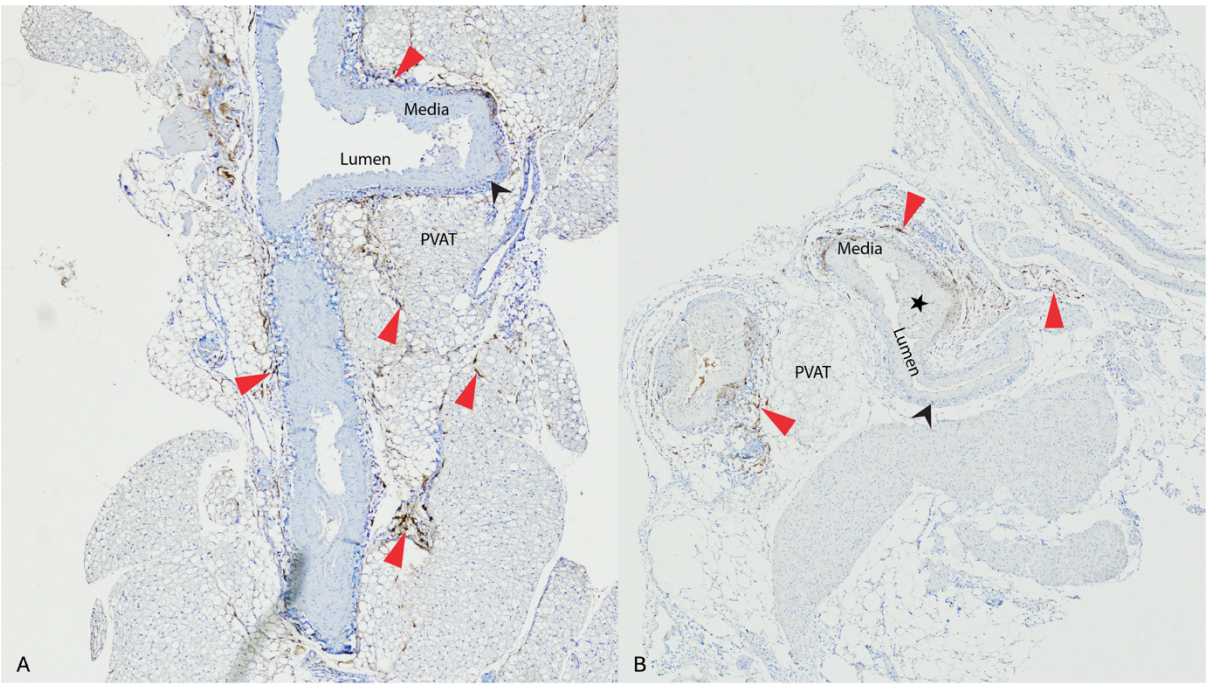

Figure 5. PI16 IHC staining on non-obese (A) and obese (B) mouse PVAT/aorta tissues. Tunica media, lumen, and PVAT are marked with text, adventitia is marked with a black arrowhead, representative PI16+ fibroblasts are marked with red arrowheads, and plaque is marked with a black star.

We had seen diminished numbers of *Pi16*+ fibroblasts in the obese PVAT-derived sample at the single-cell level but we wanted to validate this observation at the tissue level. This was done using the same IHC staining images of PI16 as mentioned above (see also data availability). Due to differences in section sizes, we calculated the number of positive cells in relation to the area (mm^2). To investigate the group differences, we fitted a generalized linear model (postoarea /100 ~ Status) with beta distribution, and then compared the estimates using a type III Anova, and finally used estimated marginal means to examine how the estimates differ from each other. The estimated group means were significantly different (P-value = 0.03804), although we observed larger variation within the obese group compared to the non-obese group (Fig 6).

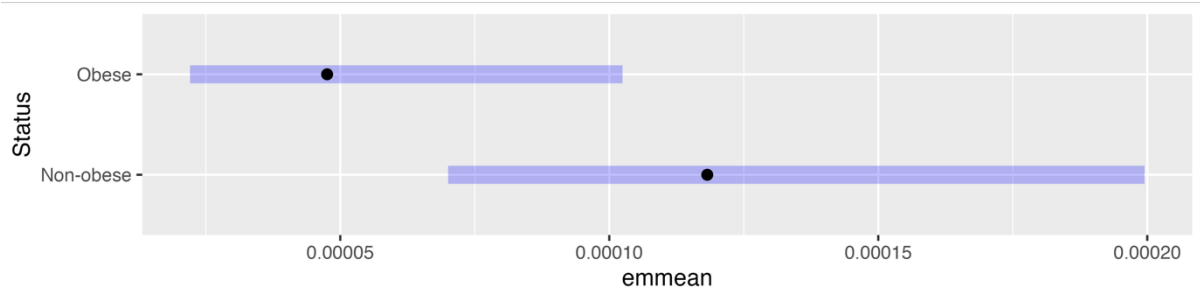

Estimated marginal means

Status	mean	SE	df	asymp.LCL	asymp.UCL
Non-obese	1.18e-04	3.16e-05	Inf	7.00e-05	0.000199
Obese	4.76e-05	1.86e-05	Inf	2.21e-05	0.000102

Confidence level used: 0.95
Intervals are back-transformed from the logit scale

Analysis of Deviance Table (Type III Wald chisquare tests):
group mean differences (positive counts relative to area)
Beta distribution, using a model:
positive counts to area / 100 ~ Status

	Chisq	Df	Pr(>Chisq)
Status	4.3033	1	0.03804 *

Figure 6. Group mean differences of *Pi16*+ cell counts relative to the area of tissue.

Trajectory analysis confirms Pi16+ fibroblasts as progenitors in both adipose tissues

Next, we performed a trajectory analysis to confirm the progenitor status[36] of the *Pi16*+ fibroblasts and to investigate their developmental relationship with the other fibroblast subpopulations found in the adipose tissues. For this task we used an R-package named Totem[25], which utilizes Slingshot[37]. The analysis was carried out separately for PVAT and eWAT, and the original clustering was used as a priori in the model. The pseudotime trajectory inference corroborated our hypothesis of the *Pi16*+ fibroblasts' progenitor status in both tissues (Fig 7). The cell connectivity (Fig 7 left side) in both tissues had a similar pattern, where the highest connectivity was around the cluster of *Ccl11*+ and *Mfap4*+ fibroblasts, indicating that they represent key transition state(s) in the model, while the *Pi16*+ progenitors, and the *Mgp*+ and *Il1b*+ fibroblasts were the start and end points in the trajectory, respectively.

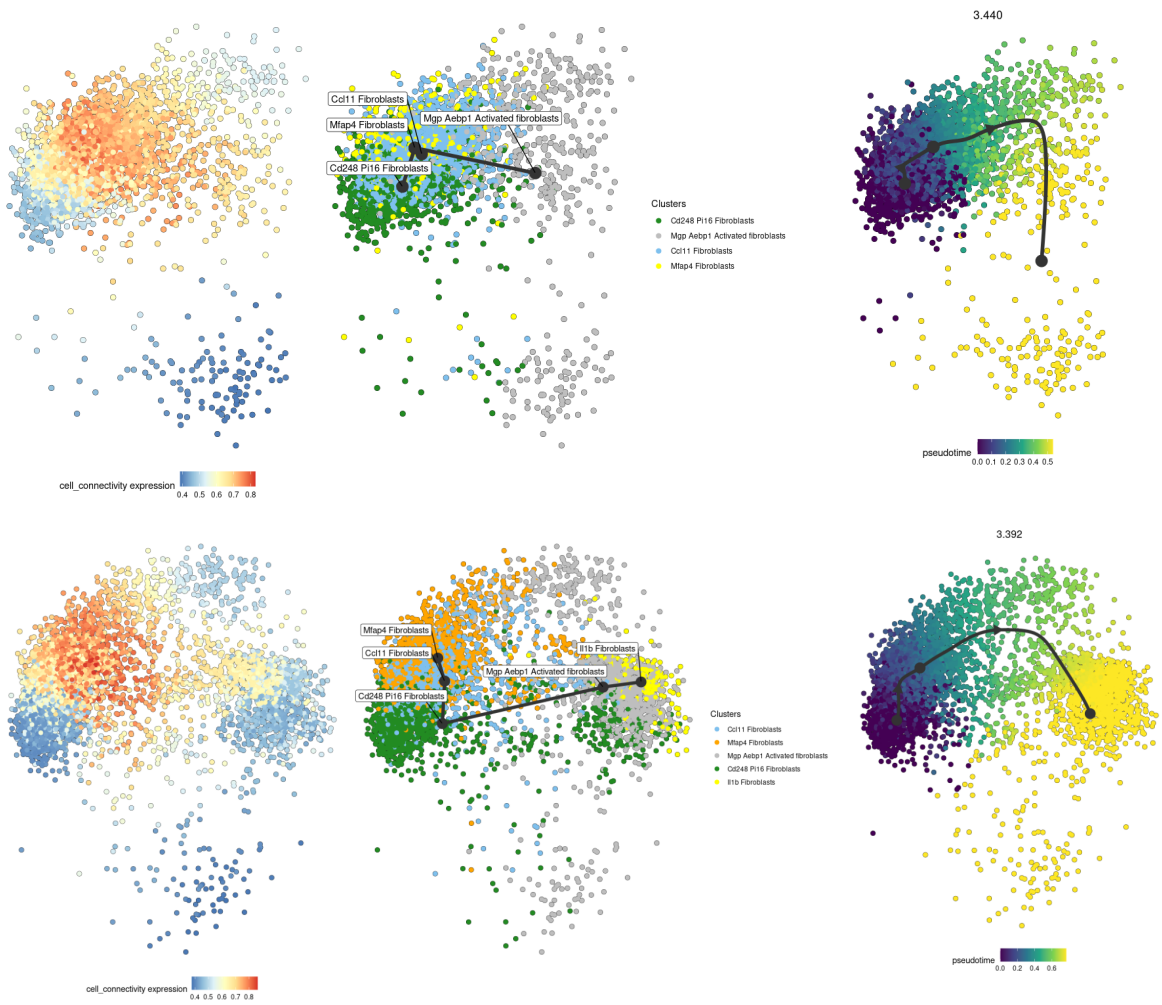

Figure 7. Cell connectivity, original clustering and pseudotime trajectory from the Totem R-package; upper image for eWAT and lower for PVAT.

Regulatory network inference analysis reveals tissue and cell-type specific regulons in adipose tissue-derived fibroblasts

Selective activation of different regulons (i.e. transcription factors and their co-regulated target genes) is considered as a major factor in determining differences in cellular activity in different tissues and disease states in complex disorders. Therefore, we carried out a regulatory network inference analysis with pySCENIC to map the transcription factors (TF) that may drive the obesity-associated states in fibroblasts and therefore impact the disease progression in the different tissues.

We found tissue and obesity state specific regulons in the different fibroblast populations, the most interesting being the *Ccl11*+ and *Pi16*+ subpopulations, having both strong tissue and obesity-state specific regulons, while for instance, *Mgp*+ fibroblasts had much less pronounced changes in their TF activity (Fig 8). The strongest regulons in the full data, based on the area under recovery curve (AUC), are depicted in Figure 8.

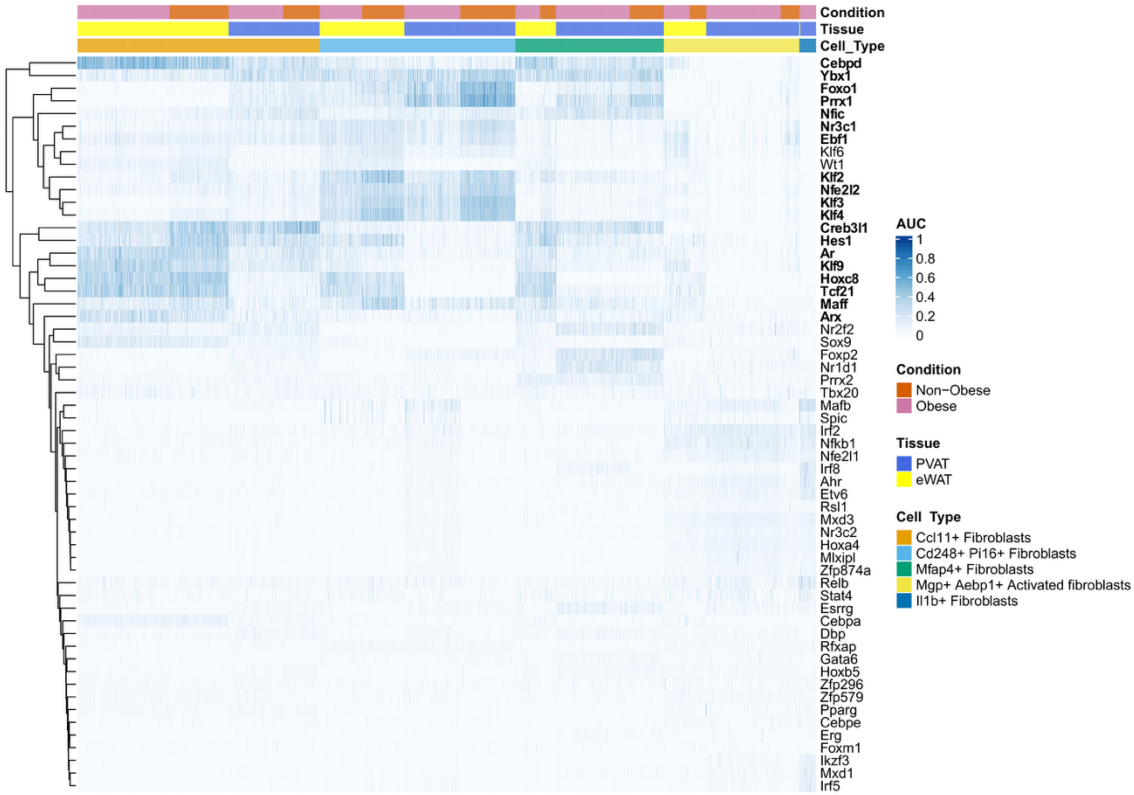

Figure 8. Heatmap of the AUC with the top regulons in all of the tissues and fibroblast subsets. The highlighted (bolded) genes are CCAAT enhancer binding protein delta (*Cebpd*), Y-box binding protein 1 (*Ybx1*), Aristaless related homeobox (*Arx*), MAF bZIP transcription factor F (*Maff*), Androgen receptor (*Ar*), Kruppel like factor 9 (*Klf9*), Homeobox C8 (*Hoxc8*), Transcription factor 21 (*Tcf21*), CAMP responsive element binding protein 3 like 1 (*Creb3l1*), Hes family BHLH transcription factor 1 (*Hes1*), Forkhead box protein 1 (*Foxo1*), Paired related homeobox 1 (*Prrx1*), Nuclear factor I C (*Nfic*), Nuclear receptor subfamily 3 group C member 1 (*Nr3c1*), EBF transcription factor 1 (*Ebf1*), Kruppel like factor 2 (*Klf2*), NFE2 like bZIP transcription factor 2 (*Nfe2l2*), and Kruppel like factors 3 and 4 (*Klf3* and *Klf4*).

Next, we investigated the *Ccl11+* and *Pi16+* fibroblasts more closely. In the *Ccl11+* fibroblasts *Cebpd*, *Tcf21*, *Hoxc8*, and WT1 transcription factor (*Wt1*) were predominantly active in the eWAT, showing no significant variation between different obesity states (Fig 9). All these genes are important for sustaining the WAT phenotype, but *Cebpd* is also an important regulator of immune and inflammatory response related genes[38]. Conversely, Forkhead box P2 (*Foxp2*), *Foxo1*, *Prrx1* were the strongest regulons in PVAT and almost non-existent in eWAT. We were also able to capture regulatory differences between obesity states in these fibroblasts (Fig 9). *Hes1* had the highest AUC score in the non-obese state in eWAT, while *Creb3l1* had high AUC scores in non-obese state in both adipose tissues.

In *Pi16+* fibroblasts the strongest regulons were *Ybx1*, *Foxo1*, *Prrx1*, and *Klf2-4* (Fig 9). Notably, all of these genes are associated with adipose differentiation, and *Ybx1* specifically with brown adipogenesis[39]. We observed that the first three are clearly more active in the non-obese state in the PVAT (*Klf2-4* also in eWAT), while *Hes1*, *Tcf21*, *Hoxc8* and *Wt1* were almost exclusively activated in the eWAT but without differences between the obesity states.

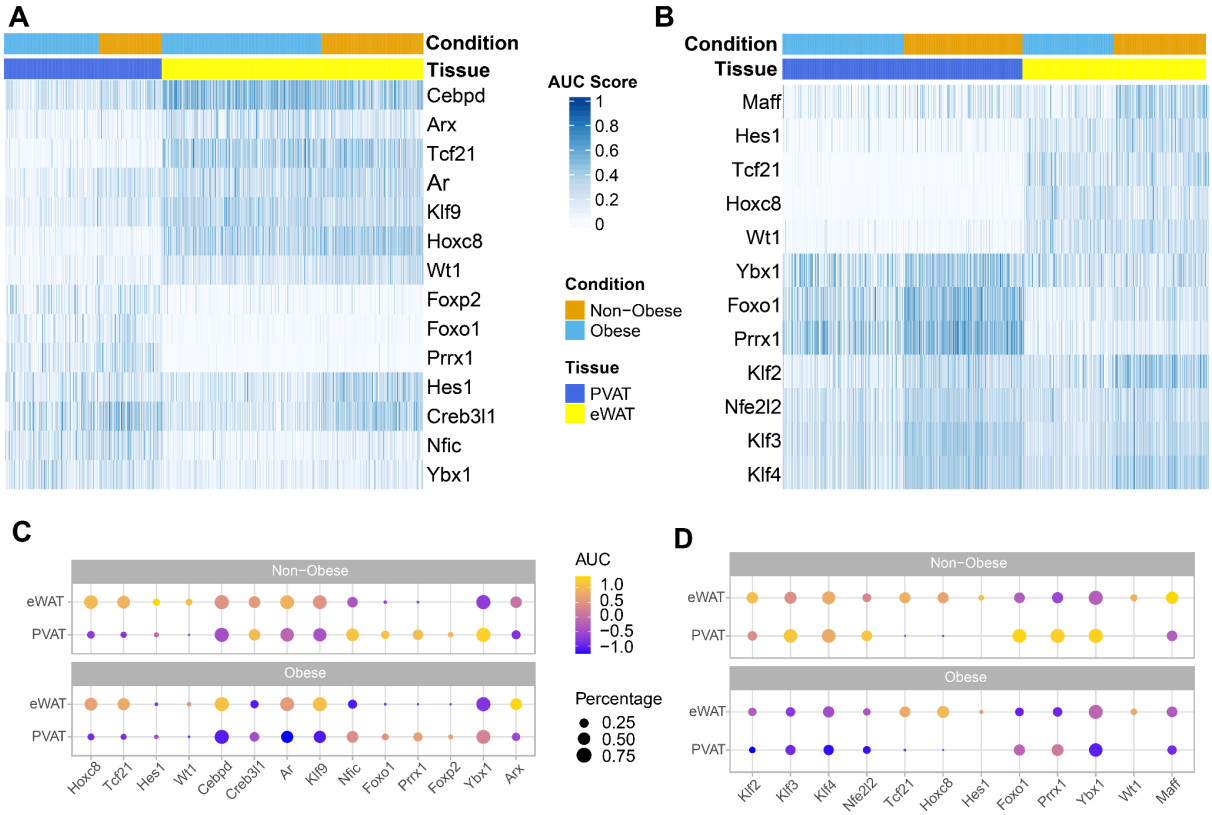

Figure 9. Heatmap and dot plot of the AUC with the top regulons in *Ccl11*+ fibroblasts (A and C) and *Pi16*+ fibroblasts (B and D) in eWAT and PVAT with the two obesity states.

Morphometric analysis reveals significant phenotype changes in PVAT

Our SCENIC analysis indicated strong modulation of adipose tissues during obesity. In line with this, we observed remarkably diverging morphology of the PVAT between the obese and non-obese mice was, potentially reflecting a pathogenic conversion[40]. In the obese mice, the PVAT showed transformation toward white adipose tissue (WAT) phenotype. We observed a shift from multilocular PVAT to more unilocular morphology, which is typical to WAT, and increased lipid accumulation was evident (Fig 10, right side), although individual differences were also seen in both groups. To quantitatively assess these differences between the groups, we carried out a morphometric analysis. Using one-way Welch t-test to evaluate whether obese mice have a greater average lipid droplet size than the non-obese mice, we observed that the difference was significant (Fig 10, left side). Interestingly, the variation in lipid droplet sizes within the obese group was much bigger than within the non-obese group, suggesting that the pace of PVAT remodeling towards the WAT phenotype can vary between individual animals even in age-matched mice.

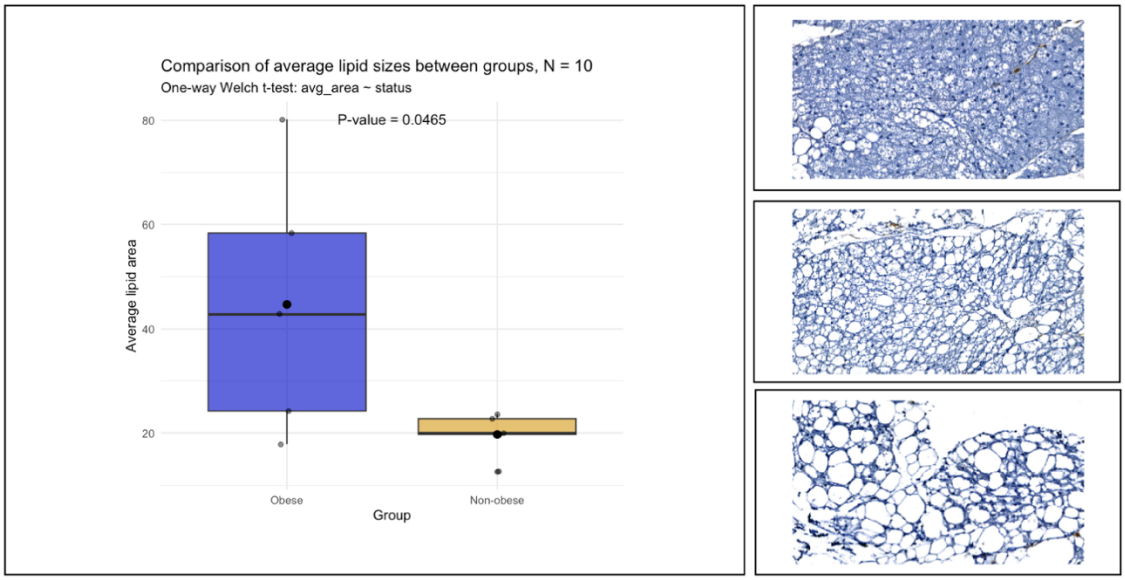

Figure 10. Average lipid size comparison between the obesity groups in the perivascular adipose tissue (left side of panel). The obese group is coloured blue and non-obese golden. Representative changes in PVAT morphology (Top: normal PVAT in a non-obese mouse, middle: PVAT with slightly abnormal WAT-like morphology in an obese mouse, bottom: PVAT with highly abnormal WAT-like morphology in an obese mouse).

PI16+ fibroblasts may interact with multiple stromal and immune cell types in adipose tissues.

Previous studies have shown that PI16 fibroblasts actively interact with endothelial cells but also with immune cells such as macrophages[41–43]. Therefore, we investigated if the PI16+ fibroblasts are co-localizing with T cells and macrophages, which would strengthen the hypothesis of their interactions in these tissues and their antigen presentation activity in our model. To achieve this, we carried out a multiplexed immunofluorescence (mIF) staining with PI16, CD3, CD4, and F4/80 (Adhesion G Protein-Coupled Receptor E1) antibodies. PI16 expression was localized in the adipose tissue and the adventitia of the aorta, as well as within plaques, resembling the PI16 IHC staining of the same tissues (Supplementary Fig 6). As expected, CD3, CD4 and F4/80 positive cells were evident in the lymph nodes, whereas the IgG isotype control showed minimal background staining (Supplementary Fig 7 and 8). Lastly, we could clearly observe that the PI16+ fibroblasts were in close proximity to both T cells and macrophages in the PVAT and the adventitia of the aorta, suggesting potential interaction between these cells (Fig 11, Supplementary Fig 8).

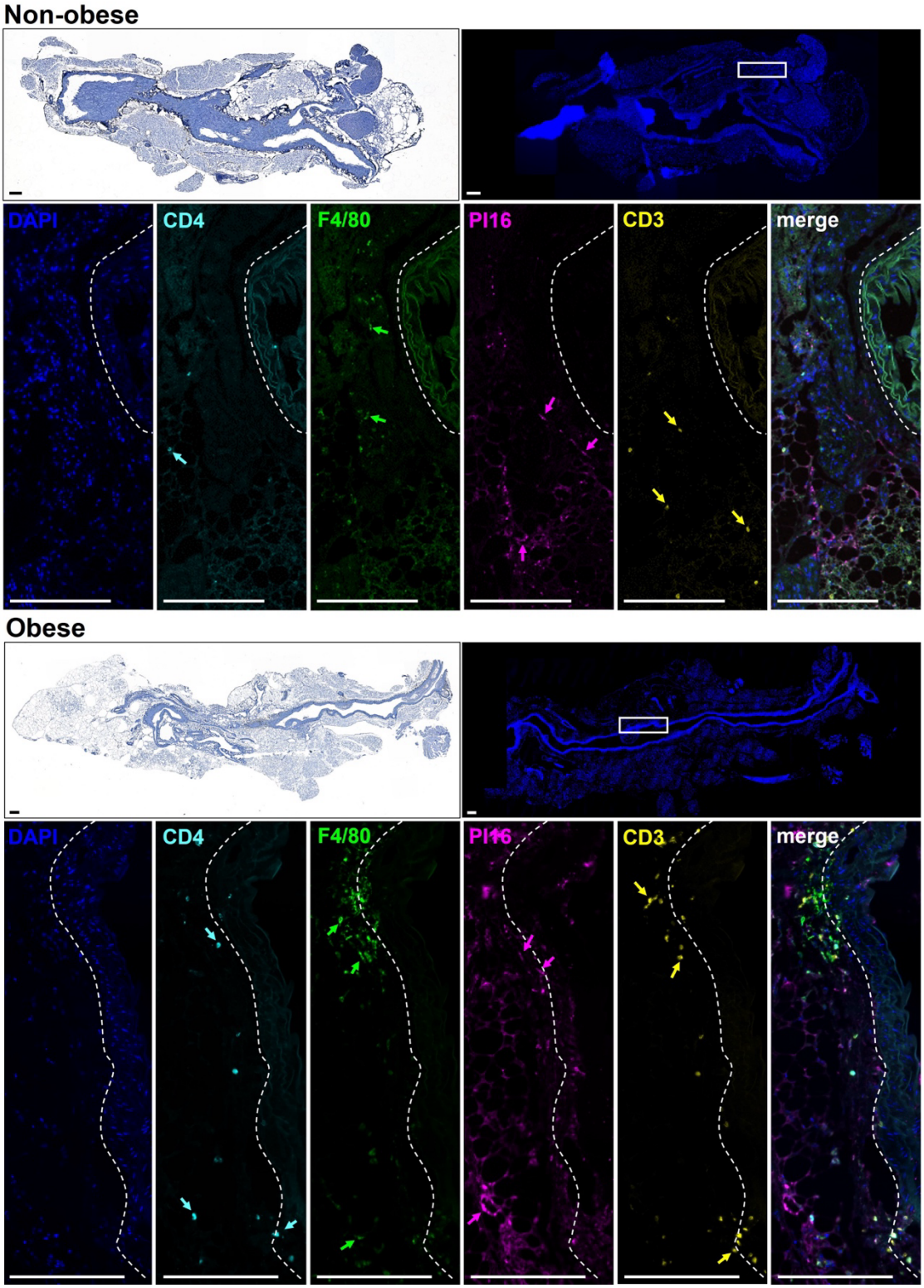

Figure 11. Multiplex immunofluorescence (mIF) staining of PI16 and multiple immune cell markers in PVAT/aorta tissue. Representative images of mIF staining in non-obese and obese mouse tissue showing CD4, F4/80, PI16 and CD3 expression in the PVAT and the adventitia of the aorta (white dashed line). Images of the PI16 IHC staining (upper left panels) depict the morphology of the mIF stained tissues (not adjacent sections). DAPI (4', 6 -diamidino-2-phenylindole) was used as nuclear counterstain. Scale bar 200 µm.

Next, we further explored other potential cell-cell interactions involved in the regulation of the PVAT-derived *Pi16+* progenitor fibroblasts. An R-package called NicheNet was used, which assesses how ligands expressed by sender cell types predict expression changes in the receiver cell type, enabling inspection of the cellular interactions not only between ligands and receptors, but also downstream target genes potentially regulated by the receptors within the receiver cells as well[28]. The *Pi16+* fibroblasts were defined as the receivers and the sender cell types were the cells that were observed in the adipose tissues and showed significant differential gene expression between the obesity states (see Methods). The Mki67 and Top2a positive cell cluster was excluded from these analyses, because it can represent multiple cell types.

The results revealed multiple general ligands and one endothelial cell specific ligand (*Vwf*; Von Willebrand Factor), that could target a set of genes downstream, which may be regulated by the receptors. The most active general ligand was *Apoe*, followed by *Tgfb2* (transforming growth factor beta 2) (Fig 12A left side) and both had multiple predicted target genes with strong regulatory potential (Fig 12B). *Apoe* was expressed to some extent in many sender cell types included in the analysis, but had strong average expression in different macrophages, while *Tgfb2* was mainly expressed by a small proportion of other fibroblast populations, and *Vwf* was only expressed by endothelial cells and some mesothelial cells (Fig 12A right side). The target genes towards which *Apoe, Tgfb2,* and *Vwf* had the highest regulatory potential are listed in Table 2. Another interesting ligand was *Il1b*. It wasn't among the most active ligands, but it showed strong regulatory potential (Fig 12B and C) with multiple target genes. In this analysis, it was most strongly expressed in a specific granulocyte population, but also by different DC and monocyte populations.

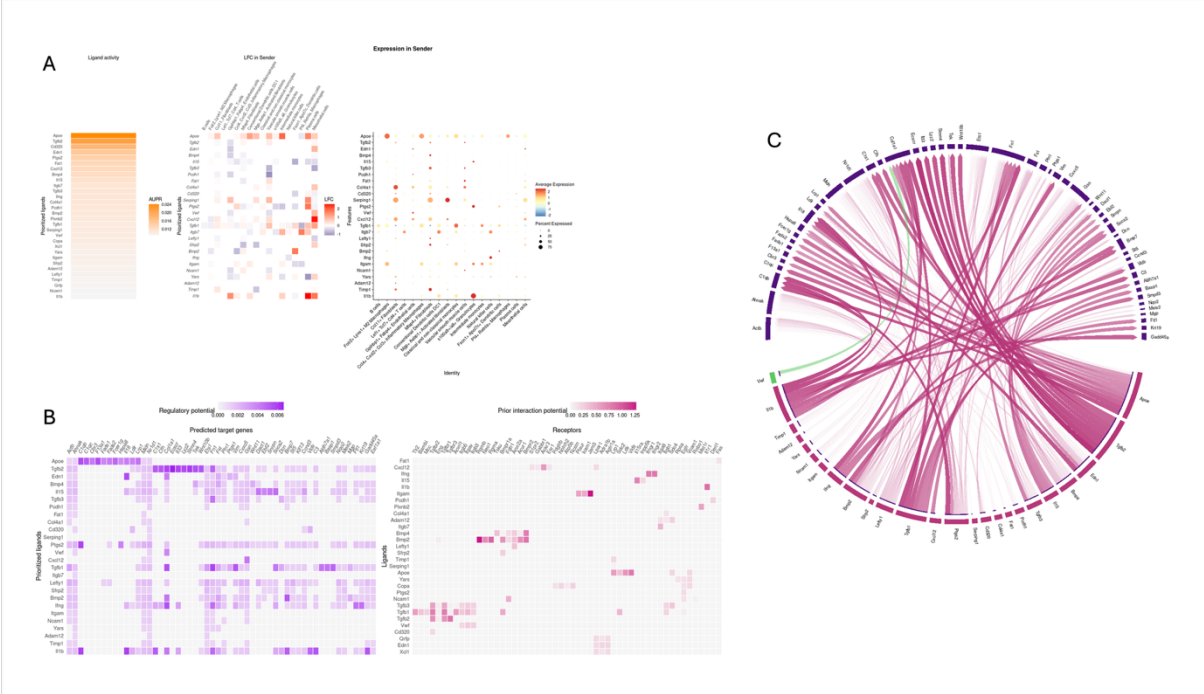

Figure 12. A) Ligand activity (left side), Log fold change in the sender cells between obesity states (middle), and gene expression in the sender cells (right side). B) regulatory potential of the predicted ligands against the predicted target genes (left side), prior interaction potential of the ligands with their respective receptors based on previous evidence (right side). C) a circos plot depicting the inferred ligand interactions with their target genes. The general ligands in the circos plot are coloured maroon, the EC-specific ligand *Vwf* is coloured light green, and the target genes are coloured purple. The stronger the regulatory potential, the stronger the line between the ligands and their targets.

Table 2. The most active ligands and their receptors and strongest target genes from the cell-cell interaction analysis.

Active ligand	**Receptors**	**Strongest target genes**
Apoe (general)	LDL receptor related protein 1 (*Lrp1*), Syndecan 2 (*Sdc2*), Low density lipoprotein receptor (*Ldlr*), Very low density lipoprotein receptor (*Vldlr*), Syndecan 4 (*Sdc4*), Vascular cell adhesion molecule 1 (*Vcam1*)	Complement C1q B chain (*C1qb*), Complement C1q C chain (*C1qc*), Carbonyl reductase 3 (*Cbr3*), Coagulation factor XIII A chain (*F13a1*), Fatty acid desaturase 1 (*Fads1*), Fatty acid desaturase 2 (*Fads2*), Fc epsilon receptor Ig (*Fcer1g*), Heat shock protein family A member 8 (*Hspa8*), Interleukin 18 (*Il18*), *Ldlr*, and *Lrp1*
Tgfb2 (general)	Transforming Growth Factor Beta Receptor 2 (*Tgfbr2*), Transforming Growth Factor Beta Receptor 1 (*Tgfbr1*), Transforming Growth Factor Beta Receptor 3 (*Tgfbr3*)	Complement component 1s (*C1s1*), Complement factor H (*Cfh*), Collagen type I alpha 1 chain (*Col1a1*), Endothelial cell surface expressed chemotaxis and apoptosis regulator (*Ecscr*), Interleukin 33 (*Il33*), Lyzozyme 2 (*Lyz2*), Stathmin 4 (*Stmn4*), TEK receptor tyrosine kinase (*Tek*), Wnt family member 10B (*Wnt10b*), and Fibronectin 1 (*Fn1*).
Il1b (general)	Interleukin 1 receptor type 1 (*Il1r1*)	*C1qb*, *Il18*, *C1s1*, *Col1a1*, *Fn1*, Bone morphogenetic protein 7 (*Bmp7*), *Vldlr*, Complement C3 (*C3*), Growth arrest and DNA damage inducible alpha (*Gadd45a*)
Vwf (endothelial cell specific)	Integrin Beta 5 (*Itgb5*), Integrin Alpha V (*Itgav*), Integrin Beta 3 (*Itgb3*)	*Col1a1*

Discussion

Together, our application of advanced 5′ single-cell RNA sequencing and rigorous validation approaches have enabled the identification of key changes within perivascular and epididymal adipose tissues in a murine model of atherosclerosis during obesity and normal weight. Driven by our data, we have focused on different fibroblast subpopulations and especially on *Pi16+* fibroblasts in this study. These fibroblasts have previously been determined as a progenitor fibroblast type[35,42], giving rise to many other fibroblasts, including myofibroblasts, and can act as a precursor for adipocyte lineage, thus playing a role in adipogenesis[42]. Our trajectory analysis confirmed this also in this atherosclerosis mouse model. However, as suggested before, *Pi16+* fibroblasts are not solely progenitors to other cell populations but can have multifaceted functions during steady state as well as in inflammation[42]. They have also been shown to promote immune cell trafficking in different contexts [41,44], and to interact with specific cytotoxic T cells and macrophages within perivascular niches in cancer[44].

Our differential gene expression analysis revealed genes that were upregulated in obesity in multiple cell types across aorta, PVAT and eWAT, such as *Cd74* and *Apoe*. Both genes have been previously strongly linked to atherosclerosis[45,46]. In humans, the production of CD74 protein is elevated in carotid atherosclerotic plaque shoulder regions, which characteristically have high macrophage accumulation, and the production of CD74 is also upregulated in vascular smooth muscle cells and monocytes under interferon gamma stimulation [47]. Indeed, we showed with our spatial transcriptomic data that the strongest *CD74* expression was in regions with accumulation of the macrophage marker *CD68* (Supplementary Fig 9). Moreover, similar CD74 expression patterns were observed in our mouse PVAT-aorta samples using IHC, where we also confirmed its expression in fibroblasts (Supplementary Fig 10). *CD74+* cancer associated fibroblasts have been shown to function as antigen presenting cells in multiple cancer types[44], while cardiac fibroblasts have been demonstrated to participate in antigen presentation and contribute to cardiac fibrosis in mouse models[48]. Our gene set enrichment analysis indicated that PVAT-derived *Pi16+* and *Mgp+* fibroblasts had antigen presentation and processing functions during obesity. Therefore, we suggest that these fibroblast populations in PVAT might act as antigen presenting cells via MHC II and could then participate in T cell mediated immune responses in atherogenic environment during obesity. Further functional studies are needed to demonstrate this *in vitro*.

Even though the role of APOE in atherosclerosis is undeniable, APOE expressing fibroblasts have not been characterized in atherosclerosis or obesity. APOE expressing fibroblasts have been indicated to play a role in the regulation of knee osteoarthritis progression[49] and have been used to define pro-inflammatory fibroblasts in skin, where they localized adjacent to vasculature[50]. To our knowledge, this is the first time *Apoe* expression has been detected in adipose tissue-derived fibroblasts in an atherosclerosis model, and its function in these cell populations warrants further research. The other cell types that had significantly increased *Apoe* expression in the obese state were an aorta-derived *Fscn1+ Apol7c+* dendritic cell population (Fascin 1 has previously been linked to migrating and mature DCs[51,52]) and PVAT-derived intermediate monocytes. Apoe deficiency has been linked with increased antigen presentation in DCs and enhanced T cell activation[53]. Apoe is important for normal

antigen presentation and processing functions of DCs via membrane lipid homeostasis; MHC II molecules concentrate in lipid rafts, which will accumulate abnormally if DCs do not express Apoe[53]. We suggest that Apoe might have a similar role in antigen-presenting fibroblasts in building lipid rafts, in which the MHC II molecules then concentrate, which could explain its upregulation in the PVAT- and eWAT-derived fibroblasts that demonstrated antigen presentation/processing potential. Moreover, in monocytes, where classical and intermediate monocytes are the main producers of APOE[54], its overexpression can lead to decreased antigen presentation capacity by monocytes[55], further highlighting APOE's importance to functional antigen presentation.

Interestingly, multiple complement cascade component genes were also upregulated in different cell types and tissues in the obese state of our mouse model. Most prominently *C4b* was upregulated in eWAT-derived *Mgp+* fibroblasts, and *C1qb* and *C1qa* in PVAT-derived *Pi16+* fibroblasts. The impact of the complement system in atherosclerosis has been previously studied quite extensively and it has been shown to have both atherogenic and -protective effects, depending on the stage of complement activation[56]. However, knowledge of local cell-specific expression is lacking, and it has been suggested to be the key to understanding how complement system drives atherosclerosis[56]. Previously, a single-cell RNA sequencing study of human atherosclerotic plaques indicated one *CD68+* myeloid cell population that had high expression of *C1QA*, *C1QB* and *C1QC*[57]. Another study showed that *C3* expression was high in VSMCs from a proximally adjacent region of a plaque from carotid artery samples[58]. We are the first to show that complement component expression might also happen in fibroblasts in the context of atherosclerosis during obesity, although this requires further validation. Moreover, we observed multiple complement cascade components expressed in the human aorta and carotid arteries with distinct spatial patterns (Supplementary Fig 11).

Another interesting finding was the enrichment of autoimmune related functions in *Mgp+* fibroblasts in PVAT in our GSE-analysis. There has been a growing interest in searching links between atherosclerosis and autoimmunity. It has been shown that autoimmune diseases, such as systemic lupus erythematosus and rheumatoid arthritis, significantly increases the risk of atherosclerosis[59,60]. However, autoimmunity mechanisms in atherosclerosis without the existence of autoimmune disorder has recently also been highlighted. For instance, Wang et al. (2023) showed that T cell tolerance, an important function that prevents autoreactivity against body's own tissues, was deteriorated in plaques, tertiary lymphoid organs in arteries, lymph nodes, and blood[61]. These findings accentuate that autoimmunity in atherosclerosis should be studied further, and we emphasize that fibroblasts should be considered as possible participants in these processes.

5' RNA sequencing enables the interrogation of the transcription start sites and therefore the study of transcription factor expression profiles. We found significant differences in multiple interesting transcription factors between the obesity states. This analysis also indicated divergent regulation programs of *Ccl11+* and *Pi16+* fibroblasts in the two adipose tissues. The strongest differences between the adipose tissue types were observed for *Cebpd*, *Tcf21*, *Hoxc8*, *Hes1,* and *Wt1*, which were expressed in the eWAT-derived fibroblasts, while minimally expressed in PVAT. This difference was pronounced in the *Pi16+* fibroblasts. *Cebpd* is an important regulator of genes that participate in immune and inflammatory responses[38], and it has a central role in early adipogenesis[62]. *Tcf21* is a white adipose tissue marker and is

implicated in contributing to the proinflammatory environment and ECM remodelling in visceral adipose tissue[63]. *Ho*xc*8* is another white adipose tissue gene, and its suppression leads to browning of white adipose tissue[64]. As with *Tcf21* and *Hoxc8*, *Hes1* and *Wt1* are also supposed to regulate white adipose tissue (WAT) formation. *Wt1* is expressed by visceral WAT, whereas subcutaneous WAT and brown adipose tissue (BAT) do not express *Wt1*[65]. Additionally, browning of eWAT is observed in *Wt1* heterozygous mice[65]. *Hes1*, which was observed to be a strong regulon in the non-obese eWAT derived *Ccl11*+ fibroblasts, is a downstream target of Notch signalling pathway and prevents browning of adipose tissue by modulating expression of *Prdm16* and *Ppargc1a*, which are important regulators of BAT thermogenesis[66]. Finally, *Creb3l1* has been indicated as an inducer of adipogenesis in a study where *CREB3L1* knockdown in human adipose-derived stem cells increased different measures of adipogenesis[67].

Two of the strongest TFs in PVAT that showed higher activity in non-obese state, *Foxo1* and *Prrx1*, are known to regulate cell proliferation and differentiation, and both have particularly been linked to mediating myofibroblast differentiation[68,69]. Moreover, *Prrx1* has been shown to be a cell stemness regulator [70] as well as to participate in adipocyte differentiation[71]. Knocking down *PRRX1* in human adipose-derived stem cells increase lipid accumulation and has been suggested to be a repressor of adipogenesis[67]. The Kruppel-like factors have been linked with a multitude of cellular processes but most interestingly they have been demonstrated to be strongly involved in adipogenesis and lipogenesis[72]. For example, myeloid-derived *Klf2* has been shown to be a key regulator of obesity, and it is downregulated during high-fat diets[73]. Our analysis also established that its expression was lower in both adipose tissues of the obese state mice across all the fibroblasts, and specifically in the *Pi16*+ fibroblasts. As a whole, the TSS analysis demonstrated that pySCENIC was able to detect the putative adipose tissue modulators in our data, and it demonstrated that the transcriptional regulation of *Pi16*+ fibroblasts had changed remarkably between the obesity states, corroborating our other findings of their switched phenotype during obesity. Further support was provided by the morphometric analysis (Fig 10), which demonstrated that the morphology of the PVAT had significantly changed. Together these results indicate that obesity has induced a remarkable shift in the PVAT functionality and has driven the progenitor as well as other fibroblasts toward immunoregulatory phenotypes, which may actively participate in immune responses in the perivascular environment.

Finally, we carried out a cell-cell interaction analysis to study how and with what cells the PVAT-derived *Pi16*+ progenitor fibroblasts might interact. *Apoe* was highlighted by this analysis once more, its target genes being, for instance, C1 complement cascade members, some essential fatty acid desaturases, low-density lipoprotein receptor proteins, and interleukin 18, which is a proinflammatory cytokine (Table 2). Complement cascade members are clearly important as already described above, and the fatty acid desaturases *Fads1* and *Fads2* are indispensable in generation of very long chain fatty acids such as Eicosapentaenoic acid and Docosahexaenoic acid, commonly known as EPA and DHA[74]. Furthermore, *Fads1* is a significant contributor in myeloid cell lipid diversity, which affects macrophage functions and activation[75], and *Fads2* is essential for proper leukotriene production during immune responses in macrophages[76].

Lipoprotein receptor signalling, represented here by *Ldlr* and *Lrp1* (and *Vldlr* as a target of the general ligand *Il1b*), has long been acknowledged to be one of the focal pathways affecting atherosclerosis development[77]. *Il18* has previously been linked with atherosclerosis plaque instability[78], and interferon gamma-dependent acceleration of atherosclerosis even in the absence of T cells[79]. *Il18* was also one of the target genes of *Il1b* in this analysis. Another interesting target for *Il1b* was *Bmp7*, which is abundant in lipid-rich plaques and can inhibit vascular calcification in mice[80] and in humans has been shown to intensify monocyte extravasation[81], a central process in atherogenesis. Generally, *Tgfb2* and *Il1b* had multifaceted targets of both immune and ECM component related genes, while complement cascade was represented again by the members *C1s1*, *Cfh* and *C3* (Table 2). *Il33*, one of the targets of *Tgfb2* has an atheroprotective effect and it has recently been suggested that this protective process could be due to inhibition of cell adhesion[82], possibly decreasing the adhesion and migration of immune cells into the arterial wall. Another atheroprotective gene, which was targeted by *Tgfb2*, was *Tek* (encoding Tie2). Deletion of *Tek/Tie2* also enhances atherogenesis by increased expression of endothelial adhesion molecules and immune cell aggregation[83].

The endothelial cell-specific ligand *Vwf* was especially intriguing, because *Pi16*+ fibroblasts have been functionally shown to interact with endothelial cells to promote transendothelial leukocyte trafficking. In *Pi16*$^{-/-}$ mice the endothelial barrier permeability to central nervous system is decreased, which leads to lower leukocyte infiltration[41], while it has been demonstrated that *Vwf* is also pivotal to endothelial permeability in blood-brain barrier[84] and vasculature[85]. It remains to be shown *in vitro*, how *Pi16*+ fibroblasts and endothelial cells may orchestrate leukocyte trafficking in atherosclerosis. Altogether the interaction analysis revealed that PVAT-derived *Pi16*+ fibroblasts may impact atherosclerosis through multifaceted roles in obesity.

Our study had some limitations. First, the lack of human adipose tissue samples; our spatial transcriptomics data included only aorta and carotid arteries without adjoining tissues, with limited number of human patients. However, we were still able to demonstrate how some of the most interesting genes from the single-cell study were expressed in the human tissues. Second, the composition of PVAT varies by region and our validation sections used for IHC and mIF mostly represented the abdominal part of the descending aorta. In the future it would be interesting to investigate if there are significant site-specific differences. Nonetheless, our single-cell data was constructed from the aorta and PVAT covering the whole aorta from the ascending aorta to the abdominal aortic region where the renal arteries diverge. Future research should concentrate on divulging functionally how *Pi16*+ fibroblasts interact with immune cells and other stromal cells, such as endothelial cells, and how they may orchestrate atherosclerosis progression or inhibition together from perivascular adipose tissues in human patients.

Altogether, we provide a comprehensive single-cell and multi-tissue perspective of the immune-stromal landscape in a murine model of atherosclerosis during obese and non-obese states. The combination of 5' single-cell RNA sequencing and rigorous validation methods defined perivascular adipose tissue-derived fibroblasts as active participants in immune regulation within the tissue, and as potential contributors to atherosclerosis through local stromal-immune interactions. Our study opens new perspectives on how obesity may exacerbate atherosclerosis via extensive changes in the PVAT functionality through different fibroblast populations, but especially by modulating the *Pi16*+ fibroblast functions.

Acknowledgements

Most of the computational work was carried out at the CSC - IT Center for Science (Finland) high performance computing system (https://research.csc.fi/service/puhti/).

We wish to thank the following core facilities of Turku Bioscience Centre (University of Turku, Finland), Univeristy of Eastern Finland (UEF), and Biocenter Finland (https://biocenter.fi/) for their invaluable services and knowledgebase that enabled the different experiments carried out in this study: Histology core facility of the Institute of Biomedicine (histology and antibody staining), Single-Cell Omics core (mIF staining), Cell Imaging and Cytometry core and Medisiina Imaging Centre (imaging, and morphometric analysis), PET-centre and Lab Animal Centre of the University of Eastern Finland (animal work), Finnish Functional Genomics Centre (sequencing services), Medical Bioinformatics Centre in Turku and Single Cell Genomics Core of University of Eastern Finland (bioinformatics consultancy).

We also extend our thanks to Dr. Milla Salonen who provided valuable insight regarding the statistical tests used in the morphometric analysis and group comparisons of PI16 activity in PVAT, and to MSc Sara Metso who helped in imaging of the IHC validation sections.

Sources of funding

Research Council of Finland (314557, 335977, 335975, 352968), InFLAMES Research Flagship Centre (337530).

Disclosures

None.

Author contributions

ML: Conceptualization, Methodology, Software, Validation, Formal analysis, Investigation, Data Curation, Visualization, Project administration, Writing - Original Draft, Writing - Review & Editing
BA: Software, Formal analysis, Visualization, Writing - Original Draft, Writing - Review & Editing
PM: Methodology, Validation, Investigation, Writing - Original Draft, Writing - Review & Editing
MI: Formal analysis, Investigation, Writing - Review & Editing
VM: Methodology, Software, Validation
FJ: Investigation, Writing - Review & Editing
HH: Investigation, Resources
SA: Investigation
HA: Investigation
PS: Conceptualization, Resources, Writing - Review & Editing
ÖT: Conceptualization, Resources, Methodology, Writing - Review & Editing
RA: Conceptualization, Resources, Funding acquisition, Writing - Review & Editing
RP: Conceptualization, Resources, Writing - Original Draft, Writing - Review & Editing

HM: Conceptualization, Funding acquisition, Writing - Review & Editing
KUM: Conceptualization, Methodology, Resources, Funding acquisition, Writing - Review & Editing
LT: Conceptualization, Methodology, Resources, Supervision, Funding acquisition, Project administration, Writing - Original Draft, Writing - Review & Editing

References

1. Örd T, Õunap K, Stolze LK, Aherrahrou R, Nurminen V, Toropainen A, Selvarajan I, Lönnberg T, Aavik E, Ylä-Herttuala S, et al. Single-Cell Epigenomics and Functional Fine-Mapping of Atherosclerosis GWAS Loci. *Circ Res* [Internet]. 2021;129:240–258. Available from: https://www.ahajournals.org/doi/full/10.1161/CIRCRESAHA.121.318971
2. Eberhardt N, Giannarelli C. How Single-Cell Technologies Have Provided New Insights Into Atherosclerosis. *Arterioscler Thromb Vasc Biol* [Internet]. 2022;42:243–252. Available from: https://www.ahajournals.org/doi/full/10.1161/ATVBAHA.121.315849
3. Roozendaal R, Mebius RE. Stromal Cell–Immune Cell Interactions. *Annu Rev Immunol* [Internet]. 2011;29:23–43. Available from: https://www.annualreviews.org/content/journals/10.1146/annurev-immunol-031210-101357
4. Noack M, Miossec P. Importance of lymphocyte–stromal cell interactions in autoimmune and inflammatory rheumatic diseases. *Nat Rev Rheumatol* [Internet]. 2021;17:550–564. Available from: https://www.nature.com/articles/s41584-021-00665-4
5. Sbierski-Kind J, Mroz N, Molofsky AB. Perivascular stromal cells: Directors of tissue immune niches. *Immunol Rev* [Internet]. 2021 [cited 2025 May 27];302:10–31. Available from: https://onlinelibrary.wiley.com/doi/10.1111/imr.12984
6. Kuret T, Sodin-Šemrl S. The Role of Fibroblasts in Atherosclerosis Progression [Internet]. In: Fibroblasts - Advances in Inflammation, Autoimmunity and Cancer. IntechOpen; 2021. Available from: https://www.intechopen.com/chapters/77138
7. Buckley CD, Pilling D, Lord JM, Akbar AN, Scheel-Toellner D, Salmon M. Fibroblasts regulate the switch from acute resolving to chronic persistent inflammation. *Trends Immunol*. 2001;22:199–204.
8. Grasset EK, Duhlin A, Agardh HE, Ovchinnikova O, Hägglöf T, Forsell MN, Paulsson-Berne G, Hansson GK, Ketelhuth DFJ, Karlsson MCI. Sterile inflammation in the spleen during atherosclerosis provides oxidation-specific epitopes that induce a protective B-cell response. *Proceedings of the National Academy of Sciences* [Internet]. 2015;112:E2030–E2038. Available from: https://www.pnas.org/doi/10.1073/pnas.1421227112
9. Witztum JL. Splenic immunity and atherosclerosis: a glimpse into a novel paradigm? *J Clin Invest* [Internet]. 2002;109:721–724. Available from: https://www.ncbi.nlm.nih.gov/pmc/articles/PMC150921/
10. Ai X-M, Ho L-C, Han L-L, Lu J-J, Yue X, Yang N-Y. The role of splenectomy in lipid metabolism and atherosclerosis (AS). *Lipids Health Dis* [Internet]. 2018;17:186. Available from: https://doi.org/10.1186/s12944-018-0841-2
11. Fuster JJ, Ouchi N, Gokce N, Walsh K. Obesity-induced Changes in Adipose Tissue Microenvironment and Their Impact on Cardiovascular Disease. *Circ Res* [Internet]. 2016;118:1786–1807. Available from: https://www.ncbi.nlm.nih.gov/pmc/articles/PMC4887147/
12. Lin A, Dey D, Wong DTL, Nerlekar N. Perivascular Adipose Tissue and Coronary Atherosclerosis: from Biology to Imaging Phenotyping. *Curr Atheroscler Rep* [Internet]. 2019 [cited 2025 May 27];21:47. Available from: https://pmc.ncbi.nlm.nih.gov/articles/PMC7172444/
13. Henning RJ. Obesity and obesity-induced inflammatory disease contribute to atherosclerosis: a review of the pathophysiology and treatment of obesity. *Am J*

Cardiovasc Dis [Internet]. 2021 [cited 2025 May 27];11:504. Available from: https://pmc.ncbi.nlm.nih.gov/articles/PMC8449192/

14. R Core Team. R: The R Project for Statistical Computing [Internet]. Available from: https://www.r-project.org/
15. Young MD, Behjati S. SoupX removes ambient RNA contamination from droplet-based single-cell RNA sequencing data. *Gigascience* [Internet]. 2020;9:giaa151. Available from: https://doi.org/10.1093/gigascience/giaa151
16. Hao Y, Hao S, Andersen-Nissen E, Mauck WM, Zheng S, Butler A, Lee MJ, Wilk AJ, Darby C, Zager M, et al. Integrated analysis of multimodal single-cell data. *Cell* [Internet]. 2021;184:3573–3587.e29. Available from: https://www.sciencedirect.com/science/article/pii/S0092867421005833
17. McGinnis CS, Murrow LM, Gartner ZJ. DoubletFinder: Doublet Detection in Single-Cell RNA Sequencing Data Using Artificial Nearest Neighbors. *Cell Syst* [Internet]. 2019;8:329–337.e4. Available from: https://www.sciencedirect.com/science/article/pii/S2405471219300730
18. Kimmel JC, Hwang AB, Scaramozza A, Marshall WF, Brack AS. Aging induces aberrant state transition kinetics in murine muscle stem cells. *Development* [Internet]. 2020;147:dev183855. Available from: https://doi.org/10.1242/dev.183855
19. Mulè MP, Martins AJ, Tsang JS. Normalizing and denoising protein expression data from droplet-based single cell profiling. *Nat Commun* [Internet]. 2022;13:2099. Available from: https://www.nature.com/articles/s41467-022-29356-8
20. Korsunsky I, Millard N, Fan J, Slowikowski K, Zhang F, Wei K, Baglaenko Y, Brenner M, Loh P, Raychaudhuri S. Fast, sensitive and accurate integration of single-cell data with Harmony. *Nat Methods* [Internet]. 2019;16:1289–1296. Available from: https://www.nature.com/articles/s41592-019-0619-0
21. Zappia L, Oshlack A. Clustering trees: a visualization for evaluating clusterings at multiple resolutions. *Gigascience* [Internet]. 2018;7:giy083. Available from: https://doi.org/10.1093/gigascience/giy083
22. Aran D, Looney AP, Liu L, Wu E, Fong V, Hsu A, Chak S, Naikawadi RP, Wolters PJ, Abate AR, et al. Reference-based analysis of lung single-cell sequencing reveals a transitional profibrotic macrophage. *Nat Immunol* [Internet]. 2019;20:163–172. Available from: https://www.nature.com/articles/s41590-018-0276-y
23. Benayoun BA, Pollina EA, Singh PP, Mahmoudi S, Harel I, Casey KM, Dulken BW, Kundaje A, Brunet A. Remodeling of epigenome and transcriptome landscapes with aging in mice reveals widespread induction of inflammatory responses. *Genome Res* [Internet]. 2019 [cited 2025 Jun 2];29:697–709. Available from: https://pmc.ncbi.nlm.nih.gov/articles/PMC6442391/
24. Kolberg L, Raudvere U, Kuzmin I, Adler P, Vilo J, Peterson H. g:Profiler—interoperable web service for functional enrichment analysis and gene identifier mapping (2023 update). *Nucleic Acids Res* [Internet]. 2023;51:W207–W212. Available from: https://doi.org/10.1093/nar/gkad347
25. Smolander J, Junttila S, Elo LL. Cell-connectivity-guided trajectory inference from single-cell data. *Bioinformatics* [Internet]. 2023;39:btad515. Available from: https://doi.org/10.1093/bioinformatics/btad515
26. de Sande B, Flerin C, Davie K, De Waegeneer M, Hulselmans G, Aibar S, Seurinck R, Saelens W, Cannoodt R, Rouchon Q, et al. A scalable SCENIC workflow for single-cell gene regulatory network analysis. *Nat Protoc* [Internet]. 2020;15:2247–2276. Available from: https://www.nature.com/articles/s41596-020-0336-2
27. Suo S, Zhu Q, Saadatpour A, Fei L, Guo G, Yuan G-C. Revealing the Critical Regulators of Cell Identity in the Mouse Cell Atlas. *Cell Rep* [Internet].

2018;25:1436–1445.e3. Available from: https://www.sciencedirect.com/science/article/pii/S2211124718316346
28. Browaeys R, Saelens W, Saeys Y. NicheNet: modeling intercellular communication by linking ligands to target genes. *Nat Methods* [Internet]. 2020;17:159–162. Available from: https://www.nature.com/articles/s41592-019-0667-5
29. Bankhead P, Loughrey MB, Fernández JA, Dombrowski Y, McArt DG, Dunne PD, McQuaid S, Gray RT, Murray LJ, Coleman HG, et al. QuPath: Open source software for digital pathology image analysis. *Sci Rep* [Internet]. 2017;7:16878. Available from: https://www.nature.com/articles/s41598-017-17204-5
30. Valkonen M, Hognas G, Bova GS, Ruusuvuori P. Generalized Fixation Invariant Nuclei Detection through Domain Adaptation Based Deep Learning. *IEEE J Biomed Health Inform*. 2021;25:1747–1757.
31. McGillycuddy M, Warton DI, Popovic G, Bolker BM. Parsimoniously Fitting Large Multivariate Random Effects in glmmTMB. *J Stat Softw*. 2025;112.
32. Hartig F. DHARMa: Residual Diagnostics for Hierarchical (Multi-Level / Mixed) Regression Models. 2024;
33. Fox J, Weisberg S. An R Companion to Applied Regression. Third. Thousand Oaks: SAGE Publications; 2019.
34. Searle SR, Speed FM, Milliken GA. Population Marginal Means in the Linear Model: An Alternative to Least Squares Means. *Am Stat*. 1980;34:216–221.
35. Angueira AR, Sakers AP, Holman CD, Cheng L, Arbocco MN, Shamsi F, Lynes MD, Shrestha R, Okada C, Batmanov K, et al. Defining the lineage of thermogenic perivascular adipose tissue. *Nat Metab* [Internet]. 2021;3:469–484. Available from: https://www.ncbi.nlm.nih.gov/pmc/articles/PMC8136151/
36. Buechler MB, Pradhan RN, Krishnamurty AT, Cox C, Calviello AK, Wang AW, Yang YA, Tam L, Caothien R, Roose-Girma M, et al. Cross-tissue organization of the fibroblast lineage. *Nature* [Internet]. 2021;593:575–579. Available from: https://www.nature.com/articles/s41586-021-03549-5
37. Street K, Risso D, Fletcher RB, Das D, Ngai J, Yosef N, Purdom E, Dudoit S. Slingshot: cell lineage and pseudotime inference for single-cell transcriptomics. *BMC Genomics* [Internet]. 2018;19:477. Available from: https://doi.org/10.1186/s12864-018-4772-0
38. Kinoshita S, Akira S, Kishimoto T. A member of the C/EBP family, NF-IL6 beta, forms a heterodimer and transcriptionally synergizes with NF-IL6. *Proc Natl Acad Sci U S A* [Internet]. 1992 [cited 2025 Jun 5];89:1473. Available from: https://pmc.ncbi.nlm.nih.gov/articles/PMC48473/
39. Wu R, Cao S, Li F, Feng S, Shu G, Wang L, Gao P, Zhu X, Zhu C, Wang S, et al. RNA-binding protein YBX1 promotes brown adipogenesis and thermogenesis via PINK1/PRKN-mediated mitophagy. *The FASEB Journal* [Internet]. 2022 [cited 2025 Sep 1];36:e22219. Available from: https://onlinelibrary.wiley.com/doi/full/10.1096/fj.202101810RR
40. Boucher JM, Ryzhova L, Harrington A, Davis-Knowlton J, Turner JE, Cooper E, Maridas D, Ryzhov S, Rosen CJ, Vary CPH, et al. Pathological Conversion of Mouse Perivascular Adipose Tissue by Notch Activation. *Arterioscler Thromb Vasc Biol* [Internet]. 2020;40:2227–2243. Available from: https://www.ahajournals.org/doi/10.1161/ATVBAHA.120.314731
41. Singhmar P, Trinh RTP, Ma J, Huo XJ, Peng B, Heijnen CJ, Kavelaars A. The fibroblast-derived protein PI16 controls neuropathic pain. *Proc Natl Acad Sci U S A* [Internet]. 2020 [cited 2025 Jun 10];117:5463–5471. Available from: https://www.pnas.org/doi/abs/10.1073/pnas.1913444117

42. McCartney EE, Chung Y, Buechler MB. Life of Pi: Exploring functions of Pi16+ fibroblasts. *F1000Res* [Internet]. 2024;13:126. Available from: https://www.ncbi.nlm.nih.gov/pmc/articles/PMC11196929/
43. De Martin A, Stanossek Y, Lütge M, Cadosch N, Onder L, Cheng HW, Brandstadter JD, Maillard I, Stoeckli SJ, Pikor NB, et al. PI16+ reticular cells in human palatine tonsils govern T cell activity in distinct subepithelial niches. *Nat Immunol* [Internet]. 2023 [cited 2025 Jun 10];24:1138. Available from: https://pmc.ncbi.nlm.nih.gov/articles/PMC10307632/
44. Gao Y, Li J, Cheng W, Diao T, Liu H, Bo Y, Liu C, Zhou W, Chen M, Zhang Y, et al. Cross-tissue human fibroblast atlas reveals myofibroblast subtypes with distinct roles in immune modulation. *Cancer Cell*. 2024;42:1764-1783.e10.
45. Li QL, Tang J, Zhao L, Ruze A, Shan XF, Gao XM. The role of CD74 in cardiovascular disease. *Front Cardiovasc Med* [Internet]. 2023 [cited 2025 Jun 12];9:1049143. Available from: https://pmc.ncbi.nlm.nih.gov/articles/PMC9877307/
46. Greenow K, Pearce NJ, Ramji DP. The key role of apolipoprotein e in atherosclerosis. *J Mol Med* [Internet]. 2005 [cited 2025 Jun 12];83:329–342. Available from: https://link.springer.com/article/10.1007/s00109-004-0631-3
47. Martín-Ventura JL, Madrigal-Matute J, Muñoz-Garcia B, Blanco-Colio LM, Van Oostrom M, Zalba G, Fortuño A, Gomez-Guerrero C, Ortega L, Ortiz A, et al. Increased CD74 expression in human atherosclerotic plaques: contribution to inflammatory responses in vascular cells. *Cardiovasc Res* [Internet]. 2009 [cited 2025 Jun 12];83:586–594. Available from: https://dx.doi.org/10.1093/cvr/cvp141
48. Ngwenyama N, Kaur K, Bugg D, Theall B, Aronovitz M, Berland R, Panagiotidou S, Genco C, Perrin MA, Davis J, et al. Antigen presentation by cardiac fibroblasts promotes cardiac dysfunction. *Nature Cardiovascular Research 2022 1:8* [Internet]. 2022 [cited 2025 Jun 13];1:761–774. Available from: https://www.nature.com/articles/s44161-022-00116-7
49. Tang S, Yao L, Ruan J, Kang J, Cao Y, Nie X, Lan W, Zhu Z, Han W, Liu Y, et al. Single-cell atlas of human infrapatellar fat pad and synovium implicates APOE signaling in osteoarthritis pathology. *Sci Transl Med* [Internet]. 2024 [cited 2025 Jun 13];16:4590. Available from: https://www.science.org/doi/10.1126/scitranslmed.adf4590
50. Solé-Boldo L, Raddatz G, Schütz S, Mallm JP, Rippe K, Lonsdorf AS, Rodríguez-Paredes M, Lyko F. Single-cell transcriptomes of the human skin reveal age-related loss of fibroblast priming. *Communications Biology 2020 3:1* [Internet]. 2020 [cited 2025 Jun 13];3:1–12. Available from: https://www.nature.com/articles/s42003-020-0922-4
51. Yamakita Y, Matsumura F, Lipscomb MW, Chou P, Werlen G, Burkhardt JK, Yamashiro S. Fascin1 Promotes Cell Migration of Mature Dendritic Cells. *J Immunol* [Internet]. 2011 [cited 2025 Jun 13];186:2850. Available from: https://pmc.ncbi.nlm.nih.gov/articles/PMC3526951/
52. Zernecke A, Winkels H, Cochain C, Williams JW, Wolf D, Soehnlein O, Robbins CS, Monaco C, Park I, McNamara CA, et al. Meta-analysis of leukocyte diversity in atherosclerotic mouse aortas. *Circ Res* [Internet]. 2020 [cited 2025 Jun 13];127:402–426. Available from: https://www.ahajournals.org/doi/10.1161/CIRCRESAHA.120.316903
53. Bonacina F, Coe D, Wang G, Longhi MP, Baragetti A, Moregola A, Garlaschelli K, Uboldi P, Pellegatta F, Grigore L, et al. Myeloid apolipoprotein E controls dendritic cell antigen presentation and T cell activation. *Nature Communications 2018 9:1*

[Internet]. 2018 [cited 2025 Jun 13];9:1–15. Available from: https://www.nature.com/articles/s41467-018-05322-1

54. Braesch-Andersen S, Paulie S, Smedman C, Mia S, Kumagai-Braesch M. ApoE Production in Human Monocytes and Its Regulation by Inflammatory Cytokines. *PLoS One* [Internet]. 2013 [cited 2025 Jul 14];8:e79908. Available from: https://journals.plos.org/plosone/article?id=10.1371/journal.pone.0079908
55. Tang Y, Zhang Y, Li X, Xu R, Ji Y, Liu J, Liu J, Zhuang Q, Zhang H. Immune landscape and the key role of APOE+ monocytes of lupus nephritis under the single-cell and spatial transcriptional vista. *Clin Transl Med* [Internet]. 2023 [cited 2025 Jul 14];13:e1237. Available from: https://pmc.ncbi.nlm.nih.gov/articles/PMC10080215/
56. Kiss MG, Binder CJ. The multifaceted impact of complement on atherosclerosis. *Atherosclerosis*. 2022;351:29–40.
57. Depuydt MAC, Prange KHM, Slenders L, Örd T, Elbersen D, Boltjes A, De Jager SCA, Asselbergs FW, De Borst GJ, Aavik E, et al. Microanatomy of the Human Atherosclerotic Plaque by Single-Cell Transcriptomics. *Circ Res* [Internet]. 2020 [cited 2025 Jun 13];127:1437–1455. Available from: https://www.ahajournals.org/doi/10.1161/CIRCRESAHA.120.316770
58. Alsaigh T, Evans D, Frankel D, Torkamani A. Decoding the transcriptome of calcified atherosclerotic plaque at single-cell resolution. *Communications Biology 2022 5:1* [Internet]. 2022 [cited 2025 Jun 13];5:1–17. Available from: https://www.nature.com/articles/s42003-022-04056-7
59. Porsch F, Binder CJ. Autoimmune diseases and atherosclerotic cardiovascular disease. *Nature Reviews Cardiology 2024 21:11* [Internet]. 2024 [cited 2025 Jun 13];21:780–807. Available from: https://www.nature.com/articles/s41569-024-01045-7
60. Sanjadi M, Rezvanie Sichanie Z, Totonchi H, Karami J, Rezaei R, Aslani S. Atherosclerosis and autoimmunity: a growing relationship. *Int J Rheum Dis* [Internet]. 2018 [cited 2025 Jun 13];21:908–921. Available from: https://onlinelibrary.wiley.com/doi/full/10.1111/1756-185X.13309
61. Wang Z, Zhang X, Lu S, Zhang C, Ma Z, Su R, Li Y, Sun T, Li Y, Hong M, et al. Pairing of single-cell RNA analysis and T cell antigen receptor profiling indicates breakdown of T cell tolerance checkpoints in atherosclerosis. *Nature Cardiovascular Research 2023 2:3* [Internet]. 2023 [cited 2025 Jun 13];2:290–306. Available from: https://www.nature.com/articles/s44161-023-00218-w
62. Hishida T, Nishizuka M, Osada S, Imagawa M. The role of C/EBPδ in the early stages of adipogenesis. *Biochimie*. 2009;91:654–657.
63. Akama T, Chun T-H. Transcription factor 21 (TCF21) promotes proinflammatory interleukin 6 expression and extracellular matrix remodeling in visceral adipose stem cells. *J Biol Chem* [Internet]. 2018;293:6603–6610. Available from: https://www.ncbi.nlm.nih.gov/pmc/articles/PMC5925812/
64. Mori M, Nakagami H, Rodriguez-Araujo G, Nimura K, Kaneda Y. Essential Role for miR-196a in Brown Adipogenesis of White Fat Progenitor Cells. *PLoS Biol* [Internet]. 2012;10:e1001314. Available from: https://journals.plos.org/plosbiology/article?id=10.1371/journal.pbio.1001314
65. Kirschner KM, Scholz H. WT1 in Adipose Tissue: From Development to Adult Physiology. *Front Cell Dev Biol* [Internet]. 2022;10. Available from: https://www.frontiersin.org/articles/10.3389/fcell.2022.854120
66. Bi P, Shan T, Liu W, Yue F, Yang X, Liang X-R, Wang J, Li J, Carlesso N, Liu X, et al. Inhibition of Notch signaling promotes browning of white adipose tissue and ameliorates obesity. *Nat Med* [Internet]. 2014;20:911–918. Available from: https://www.nature.com/articles/nm.3615

67. Ehrlund A, Mejhert N, Björk C, Andersson R, Kulyté A, Åström G, Itoh M, Kawaji H, Lassmann T, Daub CO, et al. Transcriptional dynamics during human adipogenesis and its link to adipose morphology and distribution. *Diabetes* [Internet]. 2017 [cited 2025 Jun 5];66:218–230. Available from: https://pmc.ncbi.nlm.nih.gov/articles/PMC5860264/
68. Vivar R, Humeres C, Muñoz C, Boza P, Bolivar S, Tapia F, Lavandero S, Chiong M, Diaz-Araya G. FoxO1 mediates TGF-beta1-dependent cardiac myofibroblast differentiation. *Biochimica et Biophysica Acta (BBA) - Molecular Cell Research* [Internet]. 2016;1863:128–138. Available from: https://www.sciencedirect.com/science/article/pii/S0167488915003729
69. Lee K-W, Yeo S-Y, Gong J-R, Koo O-J, Sohn I, Lee WY, Kim HC, Yun SH, Cho YB, Choi M-A, et al. PRRX1 is a master transcription factor of stromal fibroblasts for myofibroblastic lineage progression. *Nat Commun* [Internet]. 2022;13:2793. Available from: https://www.nature.com/articles/s41467-022-30484-4
70. Shimozaki K, Clemenson GD, Gage FH. Paired Related Homeobox Protein 1 is a Regulator of Stemness in Adult Neural Stem/Progenitor Cells. *Journal of Neuroscience* [Internet]. 2013;33:4066–4075. Available from: https://www.jneurosci.org/content/33/9/4066
71. Du B, Cawthorn WP, Su A, Doucette CR, Yao Y, Hemati N, Kampert S, McCoin C, Broome DT, Rosen CJ, et al. The Transcription Factor Paired-Related Homeobox 1 (Prrx1) Inhibits Adipogenesis by Activating Transforming Growth Factor-β (TGFβ) Signaling *. *Journal of Biological Chemistry* [Internet]. 2013;288:3036–3047. Available from: https://www.jbc.org/article/S0021-9258(20)46423-3/abstract
72. Wu Z, Wang S. Role of kruppel-like transcription factors in adipogenesis. *Dev Biol* [Internet]. 2013;373:235–243. Available from: https://www.sciencedirect.com/science/article/pii/S0012160612006021
73. Sweet DR, Vasudevan NT, Fan L, Booth CE, Keerthy KS, Liao X, Vinayachandran V, Takami Y, Tugal D, Sharma N, et al. Myeloid Krüppel-like factor 2 is a critical regulator of metabolic inflammation. *Nat Commun* [Internet]. 2020;11:5872. Available from: https://www.ncbi.nlm.nih.gov/pmc/articles/PMC7674440/
74. Ménégaut L, Jalil A, Thomas C, Masson D. Macrophage fatty acid metabolism and atherosclerosis: The rise of PUFAs. *Atherosclerosis* [Internet]. 2019 [cited 2025 Jul 17];291:52–61. Available from: https://doi.org/10.1016/j.atherosclerosis.2019.10.002
75. Gromovsky AD, Schugar RC, Brown AL, Helsley RN, Burrows AC, Ferguson D, Zhang R, Sansbury BE, Lee RG, Morton RE, et al. Δ-5 Fatty Acid Desaturase FADS1 Impacts Metabolic Disease by Balancing Proinflammatory and Proresolving Lipid Mediators. *Arterioscler Thromb Vasc Biol*. 2018;38:218–231.
76. Stoffel W, Holz B, Jenke B, Binczek E, Günter RH, Kiss C, Karakesisoglou I, Thevis M, Weber AA, Arnhold S, et al. Δ6-Desaturase (FADS2) deficiency unveils the role of ω3- and ω6-polyunsaturated fatty acids. *EMBO Journal* [Internet]. 2008 [cited 2025 Jul 17];27:2281–2292. Available from: https://www.embopress.org/doi/10.1038/emboj.2008.156
77. Mineo C. Lipoprotein receptor signalling in atherosclerosis. *Cardiovasc Res* [Internet]. 2019 [cited 2025 Jul 17];116:1254. Available from: https://pmc.ncbi.nlm.nih.gov/articles/PMC7243280/
78. Mallat Z, Corbaz A, Scoazec A, Besnard S, Lesèche G, Chvatchko Y, Tedgui A. Expression of interleukin-18 in human atherosclerotic plaques and relation to plaque instability. *Circulation* [Internet]. 2001 [cited 2025 Jul 16];104:1598–1603. Available from: https://www.ahajournals.org/doi/10.1161/hc3901.096721

79. Tenger C, Sundborger A, Jawien J, Zhou X. IL-18 accelerates atherosclerosis accompanied by elevation of IFN-γ and CXCL16 expression independently of T cells. *Arterioscler Thromb Vasc Biol* [Internet]. 2005 [cited 2025 Jul 17];25:791–796. Available from: https://www.ahajournals.org/doi/10.1161/01.ATV.0000153516.02782.65
80. Davies MR, Lund RJ, Hruska KA. BMP-7 is an efficacious treatment of vascular calcification in a murine model of atherosclerosis and chronic renal failure. *Journal of the American Society of Nephrology* [Internet]. 2003 [cited 2025 Jul 17];14:1559–1567. Available from: https://journals.lww.com/jasn/fulltext/2003/06000/bmp_7_is_an_efficacious_treatment_of_vascular.16.aspx
81. Sovershaev TA, Unruh D, Sveinbjørnsson B, Fallon JT, Hansen JB, Bogdanov VY, Sovershaev MA. A novel role of bone morphogenetic protein-7 in the regulation of adhesion and migration of human monocytic cells. *Thromb Res*. 2016;147:24–31.
82. Qian Z, Shaofang F, Chen C, Chunhua S, Nan W, Chao L. IL-33 Suppresses the Progression of Atherosclerosis via the ERK1/2-IRF1-VCAM-1 Pathway. *Cardiovasc Drugs Ther* [Internet]. 2024 [cited 2025 Jul 17];38:569–580. Available from: https://link.springer.com/article/10.1007/s10557-023-07523-3
83. Anisimov A, Fang S, Hemanthakumar KA, Örd T, van Avondt K, Chevre R, Toropainen A, Singha P, Gilani H, Nguyen SD, et al. The angiopoietin receptor Tie2 is atheroprotective in arterial endothelium. *Nature Cardiovascular Research 2023 2:3* [Internet]. 2023 [cited 2025 Jul 17];2:307–321. Available from: https://www.nature.com/articles/s44161-023-00224-y
84. Suidan GL, Brill A, De Meyer SF, Voorhees JR, Cifuni SM, Cabral JE, Wagner DD. Endothelial von willebrand factor promotes blood-brain barrier flexibility and provides protection from hypoxia and seizures in mice. *Arterioscler Thromb Vasc Biol* [Internet]. 2013 [cited 2025 Jun 14];33:2112–2120. Available from: https://www.ahajournals.org/doi/10.1161/ATVBAHA.113.301362
85. Hillgruber C, Steingräber AK, Pöppelmann B, Denis C V., Ware J, Vestweber D, Nieswandt B, Schneider SW, Goerge T. Blocking Von Willebrand Factor for Treatment of Cutaneous Inflammation. *Journal of Investigative Dermatology*. 2014;134:77–86.